Border Forces and Friction Control Epithelial Closure Dynamics

Olivier Cochet-Escartin, Jonas Ranft, Pascal Silberzan,* and Philippe Marcq*
Physico-Chimie Curie, Unité Mixte de Recherche 168, Institut Curie, Centre National de la Recherche Scientifique, Université Pierre et Marie Curie, Paris, France

ABSTRACT We study the closure dynamics of a large number of well-controlled circular apertures within an epithelial monolayer, where the collective cell migration responsible for epithelization is triggered by the removal of a spatial constraint rather than by scratching. Based on experimental observations, we propose a physical model that takes into account border forces, friction with the substrate, and tissue rheology. Border protrusive activity drives epithelization despite the presence of a contractile actomyosin cable at the periphery of the wound. The closure dynamics is quantified by an epithelization coefficient, defined as the ratio of protrusive stress to tissue-substrate friction, that allows classification of different phenotypes. The same analysis demonstrates a distinct signature for human cells bearing the oncogenic RasV12 mutation, demonstrating the potential of the approach to quantitatively characterize metastatic transformations.

INTRODUCTION

Epithelization, the process by which an epithelium actively covers a cell-free surface, is not only central to wound healing (1) but—encapsulating various aspects of collective cell migration—also pivotal in embryonic morphogenesis (2), regeneration, and cancer (3). Given the complexity and the diversity of processes involved after an in vivo injury (4), efforts to understand epithelization have heavily relied on cell cultures (5–8). These studies are based on the classical scratch assay, in which epithelization is triggered by physical removal of cells from the previously intact tissue. Practically, scratching is performed on confluent monolayers with pipette tips, razor blades, or laser ablation (9), which, depending on the protocol, results either in open-contour wounds (i.e., long cell-free strips that divide the initial tissue into two separate parts) or closed-contour wounds (i.e., wounds with a single continuous edge in the monolayer).

In scratch experiments, it was shown that depending on the size and geometry of the wounds and on cell type, two major, not mutually exclusive mechanisms are responsible for epithelization (10): 1), cell crawling through lamellipodial and filopodial extensions (6,8); and 2), in the case of closed-contour wounds, contraction of a continuous actomyosin ring along the wound circumference, a process referred to as purse-string closure (9,11). The two mechanisms were observed for epithelia of various cell types, for example, Madin-Darby canine kidney (MDCK) cells (7,10,12) or cornea epithelial cells (5). Furthermore, they have been observed in development, e.g., during dorsal closure of the *Drosophila melanogaster* embryo (13) or during ventral enclosure in *Caenorhabditis elegans* (14), which underlines the importance of understanding epithelization mechanisms beyond the context of wound healing.

Although the scratch assay has proved very instructive, several drawbacks have been identified with this technique. Among them are the poorly defined geometry of the initial wound, deleterious effects of the death of the removed cells, permeabilization of the border cells, and uncontrolled chemistry of the cell-free surface. Low spatial resolution is also a drawback of the laser-ablation technique, as wound geometries are here limited by the patterns of preexisting cells (9). This geometrical aspect is particularly relevant at small wound sizes, since the complex force field that develops at the free edge of the monolayer depends on the size and shape of the free area (5,12). As to the effects of physical injury of cells, not only can dead cells release various uncontrolled factors into the medium, but cells that lie at the newly formed wound edge can also be permeabilized. When studying tissue mechanical aspects, these two contributions may interfere with the release of the physical constraint. Another disadvantage of the scratch assay lies in the debris that is often left on the cell-free surface and may perturb cell migration.

To circumvent these drawbacks, another assay, called the barrier assay, which is less traumatic for the cells, has recently been proposed (15,16). This assay relies on the removal of a neutral barrier that spatially constrains the monolayer, thus triggering epithelization without destroying any cell. This concept is compatible with microfabrication techniques to allow for control of the geometry and size of wounds on the order of 1 μm (15). The barrier assay has been used to study open-contour wounds and, more recently, closed-contour wounds (12).

In this article, we study the epithelization of closed-contour wounds with a well-defined circular geometry in different epithelial cell lines. We use a barrier assay that allows us to accurately measure the closure dynamics of several tens of wounds of controlled diameter in parallel, thereby achieving high statistics. We propose a continuum-mechanics model that takes into account border

Submitted July 20, 2013, and accepted for publication November 6, 2013.

*Correspondence: pascal.silberzan@curie.fr or philippe.marcq@curie.fr

Editor: Jochen Guck.

0006-3495/14/01/0065/9 $2.00

http://dx.doi.org/10.1016/j.bpj.2013.11.015

forces, friction with the substrate, and monolayer rheology. The different parameters involved can be estimated from the experiments and a minimal model containing only the crucial ingredients can be derived. We apply this strategy to two distinct cell lines and show the existence of an epithelization parameter that controls the closure dynamics and allows a classification based on this quantitative parameter. In particular, we demonstrate the versatility of the approach by inhibiting specific pathways and quantitatively characterizing the migration phenotypes. The consequences of the expression of an oncogene in a human cell line can be quantified using the same approach.

MATERIALS AND METHODS

Cell culture

MDCK wild-type cells (17) were cultured in Dulbecco's modified Eagle's medium (Gibco, Carlsbad, CA) supplemented with 10% FBS (Sigma, St. Louis, MO), 2 mM L-glutamin solution (Gibco), and 1% antibiotics solution (penicillin (10,000 U/mL) + streptomycin (10 mg/mL), Gibco) at 37° C, 5% CO_2, and 90% humidity. The LifeAct-GFP transfected cells were prepared by usual transfection techniques with the plasmid LifeAct-GFP (Ibidi, Verona, WI), using lipofectamine, and cultured in the same medium, supplemented with 400 μg/mL geneticin (Invitrogen, Carlsbad, CA). Other derived MDCK lines used were actin-GFP (kind gift of Prof. W. J. Nelson, Stanford University, Stanford, CA), histone-mCherry, and cadherin-GFP (18). These lines were cultured in the same way as the LifeAct-GFP line.

Human embryonic kidney (HEK)-HT wild-type cells (19) were cultured in Dulbecco's modified Eagle's medium (Gibco) supplemented with 10% FBS (Sigma), 2 mM L-glutamine solution (Gibco), 1% antibiotics solution (penicillin (10,000 U/mL) + streptomycin (10 mg/mL), Gibco), 100 μg/mL hygromycin solution (Life Technologies, Carlsbad, CA) and 400 μg/mL geneticin (Invitrogen) at 37°C, 5% CO_2 and 90% humidity. The HEK-HT-RasV12 cells (19) (kind gift of Prof. C. M. Counter, Duke University, Raleigh, NC) were cultured in the same medium, supplemented with 0.5 μg/mL puromycin solution (Life Technologies).

The various inhibitors C3-transferase (Tebu-bio, Offenbach, Germany), and NSC-23766 (Tocris Bioscience, Bristol, United Kingdom) were perfused in the flow chamber for 2 h before the polydimethylsiloxane (PDMS) template was removed. We used concentrations of 1 μg/mL for C3-transferase, and 50 μM for NSC-23766.

PDMS pillars preparation

The PDMS (Sylgard 184, Dow Corning, Midland, MI) pillars were molded on a photoresist template obtained by classic photolithography techniques. Circular structures 100 and 200 μm thick were fabricated in negative photoresist (SU8-2100, Microchem, Newton, MA) by photolithography. Uncured PDMS was then poured on this template and 1 mm spacers were used to constrain the height of the whole structure. It was then cured in a 65°C oven overnight. With this technique, thousands of pillars of different radii could be manufactured at once. This PDMS stamp was then manually cut to the right dimension for each experiment.

Experimental protocol

Cells were cultured in a small-volume flow chamber (RC20-h, Warner Instruments, Hamden, CT) (Fig. S1 in the Supporting Material). The chamber was sealed at the top and bottom by No. 1 15 mm glass coverslips (Delta Scientific, Palmdale, CA). The bottom coverslip was treated with 100 μg/mL fibronectin (Life Technologies) in phosphate-buffered saline at room temperature for 1 h before being added to the chamber. The top coverslip was irreversibly bound to the PDMS template by treating both for 30 s in an air plasma. They were then both treated with poly-L-lysine-polyethylene glycol (Suso, Bloomington, IN) at 0.1 mg/mL for 5 min to ensure that cells did not adhere to the pillar side. Care was taken to protect the pillar tops from plasma oxidation so as to avoid their irreversible adhesion to the substrate when they are removed and to insure that only the pillar sides are treated with PLL-PEG. The chamber was then hermetically sealed with silicone high-vacuum grease. Cells were then seeded in the chamber at high concentrations ($\approx 5 \times 10^4$ cells/μL) and allowed to adhere for 1 h. Medium was then manually renewed every 30 min to ensure proper growth underneath the template. Under these conditions, the cells reached confluence after 6 h growth; the PDMS template was then delicately removed with the top coverslip and fresh medium was added to the chamber before imaging. We could verify that removing the pillars did not affect the fibronectin coating by using fluorescent fibronectin, and they did not perturb the cell culture, since cells cultivated on surfaces that had previously been in contact with the pillars grew homogeneously. Throughout this study, the initial time, $t = 0$, corresponds by convention to the time when the first image was acquired, unless explicitly stated otherwise.

Image acquisition and treatment

The dynamics of closure were imaged in phase contrast on an Olympus IX-71 inverted microscope equipped with thermal and atmospheric regulation (LIS, Life Imaging Service, Basel, Switzerland). Images were acquired by a CCD-camera (Retiga 4000R, QImaging, Surrey, British Columbia, Canada) and the setup was controlled by Metamorph (Molecular Devices, Sunnyvale, CA). The typical delay between two successive images was set between 3 and 15 min, depending on the initial sizes of the wounds and we used 10× and 20× objectives. Confocal imaging of either live or fixed cells was performed under an LSM 710 NLO inverted confocal microscope (Zeiss, Oberkochen, Germany) equipped with thermal and atmospheric regulation. Images were then treated using ImageJ (20) and the free surface was computed through a masking algorithm based on a Fourier filter, an edge-detection algorithm and, finally, binarization of the resulting image. This process proved robust. However, we checked by hand on several significative examples that the apparent distribution of initial radii (see Fig. 5 *A*) for a given wound size resulted from the margin of error of this technique and from intrinsic variability and not from an actual distribution of initial radii that could have been due to variations in the microfabrication process. The raw data on closure dynamics were then analyzed with Matlab (Mathworks, Natick, MA).

Circularity measurements

Wound shape was quantified by the circularity $c(t) = 4\pi S(t)/P(t)^2$, where $P(t)$ and $S(t)$ denote the perimeter and the area of the wound, respectively, at time t. This definition yields $c = 1$ for a circle, $c = \pi/4$ for a square, and in general $0 \leq c \leq 1$ for a closed curve. However, this measurement depends on the resolution of images, due to pixelization artifacts (21). We therefore normalized the circularity of each wound by its initial value, $c(t = 0)$ (Fig. S2).

Immunofluorescent stainings

Cells were fixed with 4% paraformaldehyde for 15 min, permeabilized with 0.1% Triton-X100 for 10 min, and saturated in phosphate-buffered saline supplemented with 10% FBS for 20 min. Myosin labeling was

performed by incubation for 1 h with a rabbit anti-phospho myosin light chain antibody (Ozyme, Saint Quentin Yvelines, France) at 1:100 before staining for 1 h with a Cy-3-conjugated donkey anti-rabbit (Ozyme) used at 1:500. Actin was stained with an alexa488-conjugated phalloidin (Life Technologies) at 1:1000. Finally, the cells were mounted using Gold Antifade Reagent with DAPI (Life Technologies). The samples were then imaged on an LSM 710 NLO inverted confocal microsope (Zeiss), see Fig. S3.

Laser ablation

Laser ablation experiments were performed under an LSM 710 NLO (Zeiss) inverted confocal microscope with a 64× objective. The microscope was coupled to a femtosecond-pulsed (pulse duration <100 fs) two-photon Mai-Tai HP laser (Spectra Physics, San Jose, CA). For ablation, the wavelength and output power were set at 810 nm and ~0.1 W, respectively. Between 10 and 20 iterations of the ablation were applied to a zone drawn by hand through the Zen software (Zeiss) leading to a pixel dwell between 100 μs and 200 μs.

We first performed local ablations, and recorded the time course of the retracted length of the cable (Fig. S4). Rather than using one exponentially decaying function of time, fitting by the sum of two exponentially decaying functions provided better agreement with data. The two characteristic times, one of the order of seconds and the other of the order of minutes, differed by an order of magnitude, indicative of two distinct relaxation processes (see also (22)).

To test whether the cable exerted forces inward, we performed a full ablation of the cable (Fig. S5): the entire edge of the wound retracts, with a single relaxation time >1 min. We thus hypothesize that for local ablation, the longer timescale arises from relaxation at the scale of the tissue, whereas the shorter one pertains to the linear retraction of the cable. After ablation, the circumferential cable reassembles on a timescale of the order of 10 min.

Together these observations show that the cable exerted inward forces and thus could contribute to force generation during closure.

Measurements at the scale of the epithelium

The velocity fields around the wounds were obtained through correlation-based particle image velocimetry analysis (23). The center of mass of the wound was determined at each time with ImageJ to compute the radial averages. Our measurement is consistent with a radial velocity component decaying as $1/r$ (see Fig. 3 *B;* see also Eq. S5).

The correlation length of the epithelial velocity field, as plotted in Fig. S6, was measured independently using a microstencil assay. Briefly, a few (two to four) bands of epithelium (size 1 mm × 3 mm) are allowed to migrate by releasing the microstencil. The velocity field is measured by particle image velocimetry during the first 10 h of migration after release, excluding the edges of the tissue (23). The spatial velocity correlation function was computed and averaged over angle, time, and bands. Fitting the averaged correlation function to an exponentially decaying function yielded the correlation length. In Rho$^-$ and Rac$^-$ assays, inhibitors were added 2 h before stencil removal at concentrations identical to those used in wound-healing assays.

To measure the epithelial cell density, we used a cell line constitutively expressing histone-mCherry to label nuclei (see Fig. 3, *C* and *D)*. Using Matlab, the position of the center of each nuclei was then determined. To create a density map, the map of the centers of the nuclei was convoluted by a 100 μm × 100 μm window, with care taken to avoid the cell-free patches. For each pixel, we thus computed the number of nuclei found in this 100-μm-wide window around that pixel divided by the surface of the intersection of this window with the tissue. The automated nucleus detection algorithm also allows for a simple count of the number of cells in the field of view at any time point.

RESULTS

Experiment

The experiments relied on the constraint of epithelial growth by cylindrical PDMS pillars whose base, of radius R_w, was in contact with the surface of a glass coverslip, thus preventing cell growth in these areas (Figs. 1 and S1). Removing the pillars (barriers) yielded a continuous cell monolayer surrounding circular cell-free patches, or wounds, with a surface chemistry identical to the rest of the substrate. Pillar removal did not injure the cells but triggered their migration into the cell-free regions (12,15). The free surface area, $S(t)$, of each wound was dynamically monitored and we defined an effective radius $R(t) = \sqrt{S(t)/\pi}$, from which the margin velocity was computed. Experiments were first carried out on the well-known MDCK cells that are prototypical of a cohesive epithelium (24). We then studied the influence of an oncogenic transformation on epithelization for the human embryonic kidney (HEK) line (25).

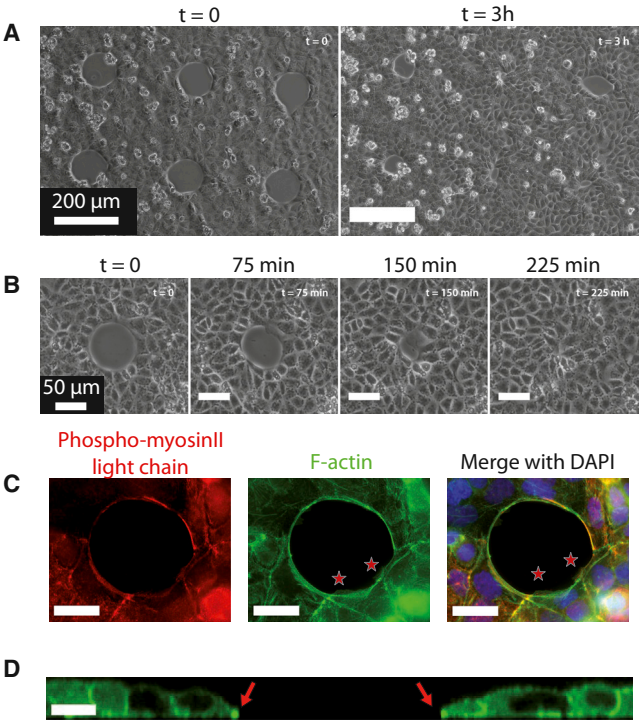

FIGURE 1 Epithelization of small circular wounds (wild-type MDCK cells). (*A*) Field of view (R_w = 50 μm). Between two and four such fields are recorded in a typical experiment. Several adjacent MDCK wounds are visible at t = 0 (*left*) and t = 3 h (*right*) after removal of the PDMS pillars. Note the intrinsic diversity of closure dynamics. The typical cell size is of the order of 15 μm. (*B*) Timelapse zoomed on a single wound (R_w = 37.5 μm). (*C*) Wound fixed at t = 30 min (R_w = 25 μm) and stained for phosphomyosin II light chain (*red*), F-actin (*green*), and nuclei (*blue*) by immunofluoresence. Note the presence of a pluricellular actomyosin cable and of lamellipodia (*stars*). For this size, we observed between zero and two lamellipodia whose area ranged between 20 and 175 μm^2 (N = 10). Scale bars, 20 μm. (*D*) Section of a live wound (MDCK-LifeAct-GFP, R_w = 25 μm, t = 30 min) imaged by confocal microscopy. The position of the cable on both sides is indicated by arrows. Scale bar, 25 μm.

MDCK circular wounds of initial radii between 100 μm and 250 μm rapidly lost their circular shape through the formation of leader cells at several positions around the margin (Movie S1). Subsequently, these leader cells dragged multicellular fingers (8,18) that eventually merged within the wound, thereby creating smaller secondary holes. These holes then proceeded to close, this time without leader cells or roughening of the margin (Movie S2). When $R_w > 100$ μm, this assay is therefore qualitatively identical with barrier assays performed on large wounds of rectangular shape (15). In contrast, smaller wounds ($R_w \leq 100$ μm) healed without the formation of leader cells, with only minor distortions of their disklike shape (Figs. 1 and S2). Of note, the observed radius of transition between these two behaviors is of the same order (100 μm) as the epithelial velocity correlation length (23).

Two possible force-generation mechanisms

We focus in the following on the closure of smaller wounds, which was completed within 20 h and presented two striking features (Fig. 1, *C* and *D*). 1), Confocal imaging of F-actin revealed lamellipodia in variable number and size at the margin (Movie S3). Active protrusions were not limited to the free surface of the wounds. We also systematically observed cryptic lamellipodia (7) within the tissue, but contrary to the protrusions at the margin, they did not show a preferential orientation (Movie S6). 2), A pluricellular actomyosin cable was assembled at the margin only minutes after removal of the pillars and ran continuously along the wound edge.

The actomyosin cable was probed with two-photon laser ablation experiments (see Methods). Local ablations induced a retraction of the severed ends of the cable (Fig. S4) on a timescale of a few seconds. This observation confirmed that the cable was under tension, as expected from the colocalization of F-actin in the cable with its associated molecular motor myosin II. Furthermore, we observed a small backward displacement (1–2 μm) of the edge of the wound in the radial direction upon ablation of the entire cable, on a timescale of a few minutes (Fig. S5 and Movie S7). Together, these results show that the cable exerts centripetal forces on the closing epithelium.

To substantiate a physical model of epithelization, we used selective inhibition to uncouple the contributions made by the contractile cable and by protrusive activity. Actomyosin contractility and lamellipodial activity are associated with the small G-proteins Rho and Rac1, respectively (26). Whereas the Rho inhibitor c3-transferase had little influence on the closure times (Fig. S7 *A*, *red curves*), the Rac1 inhibitor NSC-23766 induced a significant slowing down of the closing process (Figs. 2 *A*, *blue curves*, and S7 *B*, *black curves*). Some Rac$^-$ MDCK wounds of large enough initial radii did not close (7), and epithelization stopped at a final nonzero value of the radius, R_e (Fig. 2 *B* and Movie S8). We conclude from these results that lamellipodial activity is the dominant driving force of epithelization (6,12).

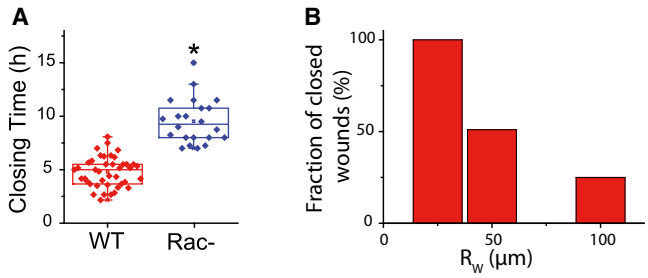

FIGURE 2 Effect of Rac1-inhibitor on closure dynamics. (*A*) Closure time ($R_w = 50$ μm) in MDCK wild-type (*red*) and Rac$^-$ (*blue*) assay. Rectangular boxes show the first quartile, the median, and the last quartile. (*B*) Rac$^-$ assay, fraction of MDCK wounds proceeding to full closure within 18 h for initial sizes of $R_w = 25$ μm ($N = 8$), $R_w = 50$ μm ($N = 39$), and $R_w = 100$ μm ($N = 16$). To see this figure in color, go online.

Epithelial velocity and cell density

Using velocimetry techniques (25,27), we measured the velocity field around circular wounds in space and time (Fig. 3 *A*). Strikingly, the angle-averaged radial component of the velocity decayed as the inverse of the distance r to the initial center of the wound (Fig. 3 *B*), a signature of monolayer incompressibility (Model in the Supporting Material). Indeed, the cell density was approximately uniform (Fig. 3 *E*), and increased by $<10\%$ during closure, since cells divided little or not at all (Fig. 3 *F*). This observation is consistent with typical cell division times of the order of the duration of closure (≈ 10 h) for the relevant cell densities (28).

Physical model of closure

Regarding the interpretation of the observations, a unified theoretical description of the involved processes is still lacking (29–31), perhaps as a consequence of the lack of reproducibility in epithelization experiments. On the basis of all experimental observations, we model the tissue as a two-dimensional, isotropic, continuous material, whose flow is incompressible and driven by border forces (Model in the Supporting Material). The epithelium occupies at time t the space outside a disk of radius $R(t)$, with an initial radius $R_0 = R(t = 0)$ (Fig. 4 *A*). We assume that lamellipodia exert a constant protrusive stress, σ_p, at the margin, and that the friction force between epithelium and substrate is proportional to the velocity, with a friction coefficient ξ. The radial force balance equation is integrated with a boundary condition at a (maximal) cutoff radius $r = R_{max}$, a parameter of the model. A differential equation for $R(t)$ follows from the stress boundary condition at the border. Neglecting the contribution of the peripheral cable to force generation,

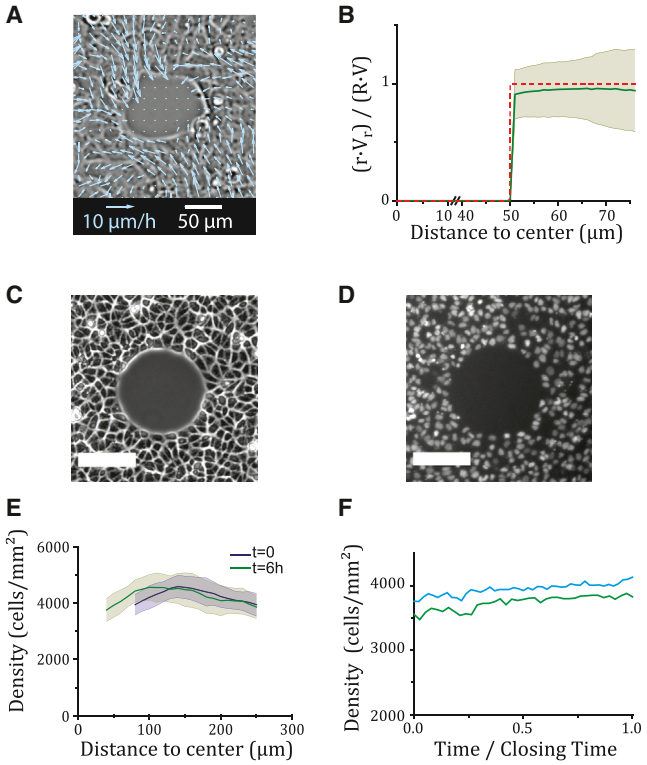

FIGURE 3 Measurements at the scale of the epithelium. (*A*) Snapshot of the epithelial velocity field (wild-type MDCK wound, $R_w = 50$ μm, $t = 1$ h). (*B*) Plot of the ensemble-averaged ratio $\langle r\, V_r / R\, V \rangle_N$ versus radius, r (*solid green line*, $N = 21$), where V_r is the angle-averaged radial velocity component, and $R(t)$ and $V(t) = \dot{R}(t)$, respectively denote the effective margin radius and velocity. The shaded area gives the mean ± SD. The radial velocity profile of an incompressible epithelial flow reads $rV_r(r,t)/(R(t)V(t)) = 1$ (Eq. S5), plotted as a dashed red line for comparison. (*C* and *D*) Phase-contrast (*C*) and epifluorescence (*D*) views of MDCK cells expressing histone-mCherry. Scale bar, 100 μm, $R_w = 75$ μm. (*E*) Radial cell density profile at $t = 0$ h and $t = 6$ h. The shaded areas give the mean ± SD. (*F*) Plot of the mean cell density in the entire field of view as a function of time for two wounds ($R_w = 75$ μm). The relative increase in density is of the order of 10% during closure.

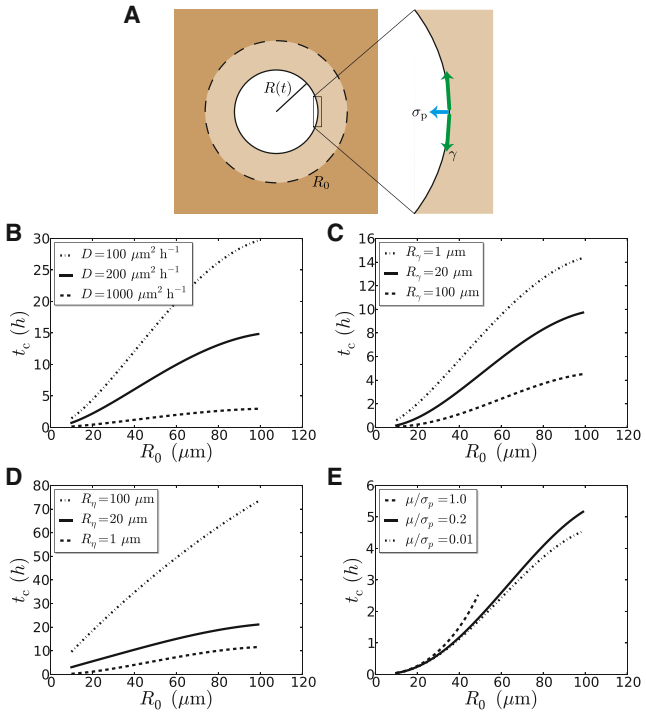

FIGURE 4 Physical model of epithelial closure. (*A*) Sketch of a closing circular wound, of initial radius $R_0 = R(t = 0)$. Two border forces may drive closure: σ_p is the protrusive stress produced by lamellipodia and γ the line tension due to the contractile circumferential cable (see the stress boundary condition (Eq. S4)). (*B–F*) Model predictions. Plots of the closure time, t_c, as a function of the initial effective radius, R_0. (*B*) Effect of the variation of D while $R_{max} = 110$ μm is fixed, inviscid rheology without cable (Eqs. 1 and S27). (*C*) Effect of the variation of $R_\gamma = \gamma/\sigma_p$ while $D = 200$ μm^2 h^{-1} and $R_{max} = 110$ μm are fixed, inviscid rheology with a cable (Eq. S28). (*D*) Effect of the variation of $R_\eta = \sqrt{\eta/\xi}$ while $D = 200$ μm^2 h^{-1}, $R_{max} = 110$ μm, and $R_\gamma = 10$ μm are fixed, viscous rheology (Eq. S29). (*E*) Effect of the variation of μ/σ_p while $D = 200$ μm^2 h^{-1}, $R_{max} = 110$ μm, and $R_\gamma = 100$ μm are fixed, elastic rheology (Eq. S30). When $\mu/\sigma_p = 1$, closure is complete and characterized by a finite closure time only below a value of R_0 above which elastic forces are strong enough to stop epithelization. To see this figure in color, go online.

and using an inviscid tissue rheology, we obtain an analytical expression for the closure time $t_c = t(R = 0)$ as a function of the initial radius, R_0 (Eq. S12):

$$t_c(R_0) = \frac{R_0^2}{4D}\left(1 + 2\ln\left(\frac{R_{max}}{R_0}\right)\right), \qquad (1)$$

where the epithelization coefficient $D = \sigma_p/\xi$ has the dimension of a diffusion coefficient.

Data analysis

Since the closure time is a robust quantity that depends little on the specifics of image analysis, we used Eq. 1 to fit the data and measure the parameters σ_p/ξ and R_{max} (Figs. 5 and S8). Of note, the experimental data plateau for $R_0 \gtrsim 100$ μm. This behavior is not consistent with a simple scaling relationship where the closure time would be proportional to the initial area πR_0^2, as proposed in (12) (Fig. S8, *insets*). We checked that taking into account force generation by the actomyosin cable in the stress boundary condition does not modify our results (Data analysis in the Supporting Material, and Fig. S9 *A*). We found that the cutoff radius, R_{max}, of the order of 110 μm, varied little between different conditions. Compared to its wild-type value ($D_{wt} = 353 \pm 38$ μm^2 h^{-1}, $N = 130$), the epithelization coefficient was strongly reduced by Rac inhibition ($D_{Rac} = 198 \pm 22$ μm^2 h^{-1}, $N = 34$) and adopted an intermediate value under Rho inhibition ($D_{Rho} = 278 \pm 40$ μm^2 h^{-1}, $N = 30$). Furthermore, individual trajectories of wound radii were satisfactorily fitted by the predicted time evolution of the radius, $R(t)$ (Eq. S11 and Fig. 6 *C*), and yielded estimates of the epithelization coefficient consistent within error with those obtained from closure-time data, albeit with larger uncertainties

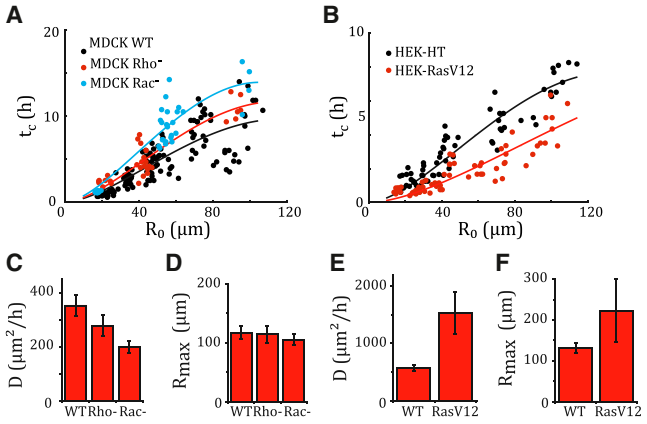

FIGURE 5 Physical parameters of epithelization. (*A* and *B*) Closure time t_c (*solid circles*) as a function of the initial effective radius, R_0, fitted by Eq. 1 (*solid curves*) with the constraints $D, R_{max} \geq 0$. Each circle corresponds to one wound. (*A*) MDCK wounds. Wild-type ($D = 353 \pm 38\ \mu m^2\ h^{-1}$, $R_{max} = 117 \pm 11\ \mu m$, $N = 130$), Rho$^-$ assay ($D = 278 \pm 40\ \mu m^2\ h^{-1}$, $R_{max} = 114 \pm 9\ \mu m$, $N = 30$), and Rac$^-$ assay ($\sigma_p/\xi = 198 \pm 22\ \mu m^2\ h^{-1}$, $R_{max} = 105 \pm 11\ \mu m$, $N = 34$). (*B*) HEK-HT assay ($\sigma_p/\xi = 572 \pm 57\ \mu m^2\ h^{-1}$, $R_{max} = 132 \pm 12\ \mu m$, $N = 653$) and HEK-RasV12 assay ($\sigma_p/\xi = 1531 \pm 363\ \mu m^2\ h^{-1}$, $R_{max} = 223 \pm 77\ \mu m$, $N = 65$). (*C–F*) Epithelization coefficient, D, and cutoff radius, R_{max}, for MDCK (*C* and *D*) and HEK wounds (*E* and *F*). Error bars correspond to a 95% confidence level.

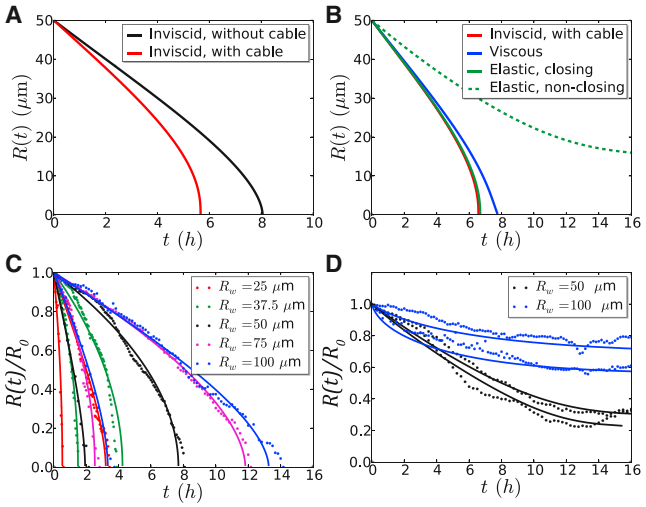

FIGURE 6 Trajectories. Model predictions: Plots of individual trajectories of the wound radius $R(t)$, $R_0 = 50\ \mu m$. (*A*) Contribution of border forces for an inviscid fluid. Plots of $R(t)$ as given by Eq. S11, $D = 200\ \mu m^2\ h^{-1}$, $R_{max} = 110\ \mu m$ (without cable, *black curve*); and Eq. S10, with the same values of D and R_{max}, $R_\gamma = 10\ \mu m$ (with cable, *red curve*). (*B*) Rheology. Plots of $R(t)$ as given by Eq. S10 (inviscid liquid, as in *A* (*red curve*)); Eqs. S16 and S17, with $R_\eta = 10\ \mu m$ (*blue curve*, viscous liquid); Eqs. S23 and S24, with $2\mu/\sigma_p = 0.1$ (*solid green curve*, elastic solid, closing); Eq. S26, with $R_e = 15\ \mu m$ (elastic solid, nonclosing, *dashed green curve*,); The values of D, R_{max}, and R_γ are the same as in *A*. Experimental data and fits (*C*) Normalized effective radius, $R(t)/R_0$, is plotted as a function of time t for MDCK wild-type wounds. For clarity, we show only two trajectories (*circles*) and their fits by Eq. S11 (*solid curves*) per pillar size, R_w, corresponding to the shortest and longest closure time observed at a given R_w. (*D*) Normalized effective radius, $R(t)/R_0$, is plotted as a function of time t for nonclosing wounds of the MDCK Rac$^-$ assay. For illustrative purposes, we show only two trajectories $t(R)$ per pillar size R_w (*solid curves*) and their fit by Eq. S26 (*dashed curves*), with the constraints $D_s \geq 0$, $R_{max} \in [96,114]\ \mu m$ (confidence interval obtained from closure-time data) and $R_c = \min R(t)$. Note that (Eq. S26) is defined only for $R > R_e$.

(Fig. S10). Since Rac inhibition impairs actin polymerization at the leading edge of migrating cells (26), one expects a lower protrusive stress in Rac$^-$ assays, conducive to a lower value of σ_p/ξ. Both Rac and Rho inhibition may also modify the friction coefficient, ξ, which generally depends on the intensity and the dynamics of cell-substrate adhesion. This may explain the lower value of σ_p/ξ measured under Rho inhibition.

To check whether our results were robust when changing model assumptions on the epithelial rheology, we investigated the predicted closure dynamics of 1), a viscous epithelium, with shear viscosity coefficient η; and 2), an elastic epithelium, with shear elastic modulus μ. Fitting data with the more complex functional forms of $t_c(R_0)$ thus obtained (Model in the Supporting Materiral, and Fig. 4, *D* and *E*), we concluded that 1), $\xi R_0^2/\eta \gg 1$, with external friction dominating internal viscosity (32); and 2), $\sigma_p/\mu \gg 1$, with protrusive forces dominating elastic forces (Data analysis in the Supporting Material). These results confirm that Eq. 1 provides a satisfactory description of the data on closing wounds. Further, the trajectories of nonclosing Rac$^-$ wounds could be fitted with the analytical expressions obtained on the basis of an elastic epithelial rheology (Figs. 6 *D* and S11). Due to Rac inhibition, the border force was small enough to allow a restoring elastic force to stop epithelization on the timescale of the experiment.

HEK cells

Finally, to test the sensitivity of the proposed quantification to cell phenotypes, we studied and compared epithelization by HEK-HT cells and by the derived cell line constitutively expressing the H-Ras oncogene, HEK-RasV12, using the same experimental and data analysis protocols. The dynamics were globally faster than what had been observed for MDCK cells (compare Movies S3 and S4 and Fig. 5, *A* and *B*). Moreover, the HEK-RasV12 cell line had a greater protrusive activity than the HEK-HT line (compare Movies S4 and S5). The model in its simplest form (Eq. 1) accounted well for the closure-time data (Fig. 5 *B*). Further, HEK-RasV12 wounds were characterized by a larger epithelization coefficient ($D_{HEK-RasV12} = 1531 \pm 363\ \mu m^2\ h^{-1}$, $N = 65$) compared to HEK-HT wounds ($D_{HEK-HT} = 572 \pm 57\ \mu m^2\ h^{-1}$, $N = 63$). The mutation carried by the HEK-RasV12 cell line is known to be common in different types of cancer (33) and to promote angiogenesis (34) and cell motility (35). That the value of the epithelization coefficient for HEK-RasV12 is larger than that for HEK-HT wounds proves to be a signature of the metastatic capacity of the transformed cell line. Thanks to our experimental and data analysis protocols, the kinetics

of closure translates into the measurement of a mechanical parameter whose value may allow discrimination of the collective migration phenotypes of various cell types and conditions in screening assays.

Physical parameters

The epithelization coefficient, $D = \sigma_p/\xi$, estimated for wild-type MDCK wounds was of the order of 350 $\mu m^2\ h^{-1}$, or 10^{-1} $\mu m^2\ s^{-1}$. Using the order of magnitude of cell protrusive forces, $F_p \approx 1$ nN (36), the two-dimensional protrusive stress, σ_p, is of the order of F_p/L, where L is the typical lateral extension of a cell. Using $L \approx 10$ μm, we find $\sigma_p \approx 10^{-1}$ nN μm^{-1}. We then deduce the order of magnitude of the friction coefficient, $\xi \approx 1$ nN μm^{-3} s, here for a cell monolayer on a glass substrate. Interestingly, this value is consistent with that proposed in (29), using very different assumptions to model epithelization. It is also compatible with the orders of magnitude of epithelial velocities and traction forces (37,38). Down- or upregulating integrin expression or turnover may modify ξ and in turn alter epithelization dynamics. An independent measurement of the friction coefficient could test our predictions.

The second quantifier of closure dynamics is the cutoff radius, R_{max}. Since the epithelial pressure vanishes at R_{max} (Eq. S7), it may be interpreted as the lengthscale beyond which the state of the tissue is no longer modified by the presence of an open boundary. Indeed, Fig. S6 shows that a correlation exists between the cutoff radius and the epithelial velocity correlation length, as measured independently in the bulk of a cell monolayer (see Methods). As a consequence, we conjecture that R_{max} would decrease upon reducing the cohesiveness of the tissue, e.g., by downregulating cadherin expression.

DISCUSSION

Compared to wild-type MDCK assays, the epithelization coefficient, D, adopted a lower value under Rho inhibition, and was further reduced by Rac inhibition. A lower value of the ratio σ_p/ξ corresponds to a lower value of σ_p and/or to a higher value of ξ. In the case of Rac$^-$ assays, it is now well established that Rac is responsible, through the activation of the Arp2/3 complex, for actin polymerization at the leading edge of a migrating cell (39–41), which is necessary for force production by lamellipodia. The lower value of D in Rac$^-$ assays may well be explained by this effect alone. However, Rac inhibition may also modify the value of ξ: indeed the Rac pathway is also known to be involved in the formation of focal contacts (see, e.g., (42)).

On general physical grounds (43,44), a simple expression for the friction coefficient is given by $\xi = nk\tau$, where n, k, and τ denote the average density of adhesive bonds, the bond spring constant, and the average binding time, respectively. These three quantities are related to the formation of adhesive bonds, to their maturation state, and to their turnover. The influence of the Rho and Rac GTPases on these three mutally interacting biological processes is complex, often with antagonistic effects on any two of them (39–42,45). On the basis of current knowledge, predicting the effect of Rho and Rac inhibition on epithelium-substrate friction seems very difficult, all the more so since conclusions drawn from single-cell motility assays may not carry over to the case of collective migration of a cell monolayer. Still, it has been shown that Rho is not implicated in the polarization of actin at the leading edge of a migrating cell and that its inhibition can even enhance motility in certain cell types (46). We conjecture that the lower value of D in Rho$^-$ assays may be due to a higher value of ξ. This may be explained by the implication of Rho in regulating the turnover of adhesion complexes, more stable under Rho inhibition, thus leading to a higher τ and possibly to a higher ξ (45). However, existing data regarding the effect of Rho on n and k is inconclusive: for instance, it has been observed that Rho$^-$ assays lead to a lower integrin density (47). Our measurement may be seen as direct evidence for the effect of Rho inhibition on the epithelium-substrate friction coefficient and may be used as a basis toward a better understanding of the role played by the Rho GTPase in regulating the formation, maturation, and turnover of cell-substrate adhesive bonds in epithelia.

Fits of closing and nonclosing trajectories in Rac$^-$ assays showed that the epithelization coefficient is larger when closure is complete. Neglecting the cable line tension $\gamma = 0$, the equilibrium radius reads $R_e = R_0/(1 + 2\mu/\sigma_p) \geq 0$. Our model suggests that closure is incomplete as soon as $R_e > a$, where a is the cellular lengthscale below which microscale mechanisms operate to terminate epithelization (see Model in the Supporting Material). For simplicity, we ignore the possible influence of Rac inhibition on the epithelial elastic modulus, through, e.g., the dynamics and density of cell-cell adhesions (41). The condition $R_e > a$ corresponds to a threshold value $\sigma_{p,c}$ of the protrusive stress, $\sigma_p < \sigma_{p,c} = 2\mu\ (R_0 - a)/a \simeq 2\mu R_0/a$, which increases with R_0. Given the observed experimental variability, we expect the value of σ_p to fluctuate from wound to wound in a given Rac$^-$ assay. For smaller wounds, crossing the threshold $\sigma_{p,c}$ is less likely: indeed, the fraction of nonclosing wounds is an increasing function of initial radius (Fig. 2 *B*). Altogether, our analysis suggests that Rac inhibition lowers the ratio σ_p/μ so that epithelial elasticity can no longer be neglected.

CONCLUSION

To summarize, a model of the epithelium as an inviscid fluid allowed to quantify the closure of small circular wounds and to classify different cell phenotypes according to the value of the epithelization coefficient, $D = \sigma_p/\xi$, defined as the ratio of the border protrusive stress, σ_p, to the friction

coefficient, ξ, between epithelium and substrate. Altogether, the good agreement obtained between model predictions and experimental data validates the modeling assumptions we made, such as isotropy of the epithelium and rotational invariance about the initial center of the wound. On the relevant timescale of several hours, the viscoelastic rheology of the epithelium could be neglected: the protrusive force generated by lamellipodia at and close to the margin dominated force generation and drove collective migration, whereas epithelium-substrate friction dominated dissipation. The purse-string mechanism contributed negligibly to force generation and thus was not necessary for epithelization, a feature reminiscent of in vivo tissue spreading during zebrafish gastrulation (48). In the experiments presented here, the contractile cable likely played a structural role: its tension ensured a symmetric closure by rounding the shape of the wound.

Recent work has shown that the competition between friction and flow governs collective migration in developing organisms (32,48,49). Appropriate modifications of the model may lead to quantitative descriptions of in vivo epithelization during wound healing (2,11,50), but also during embryonic morphogenesis, as, for example, during the dorsal closure of *D. melanogaster* (13) or the ventral enclosure of *C. elegans* (14). Depending on the system, we expect to measure relevant quantities among the ratios σ_p/ξ, γ/ξ, γ/σ_p, η/ξ, and μ/σ_p, that quantify collective migration phenotypes through the relative importance of border forces, friction, and tissue rheology.

SUPPORTING MATERIAL

Eleven figures, eight movies, and a detailed description of the model are available at http://www.biophysj.org/biophysj/supplemental/S0006-3495(13)01245-9.

The authors thank Olivier Leroy and Olivier Renaud, along with other members of the PICT-IBISA platform, for their help with confocal imaging and laser ablation experiments, and Maria Carla Parrini for her help with immunostaining experiments.

We acknowledge support from the Association pour la Recherche contre le Cancer, and from the Labex ANR-10-LBX-0038 part of the Idex NANR-10-IDEX-0001-02 PSL.

REFERENCES

1. Sonnemann, K. J., and W. M. Bement. 2011. Wound repair: toward understanding and integration of single-cell and multicellular wound responses. *Annu. Rev. Cell Dev. Biol.* 27:237–263.
2. Wood, W., A. Jacinto, …, P. Martin. 2002. Wound healing recapitulates morphogenesis in *Drosophila* embryos. *Nat. Cell Biol.* 4:907–912.
3. Friedl, P., and D. Gilmour. 2009. Collective cell migration in morphogenesis, regeneration and cancer. *Nat. Rev. Mol. Cell Biol.* 10:445–457.
4. Gurtner, G. C., S. Werner, …, M. T. Longaker. 2008. Wound repair and regeneration. *Nature.* 453:314–321.
5. Grasso, S., J. A. Hernández, and S. Chifflet. 2007. Roles of wound geometry, wound size, and extracellular matrix in the healing response of bovine corneal endothelial cells in culture. *Am. J. Physiol. Cell Physiol.* 293:C1327–C1337.
6. Fenteany, G., P. A. Janmey, and T. P. Stossel. 2000. Signaling pathways and cell mechanics involved in wound closure by epithelial cell sheets. *Curr. Biol.* 10:831–838.
7. Farooqui, R., and G. Fenteany. 2005. Multiple rows of cells behind an epithelial wound edge extend cryptic lamellipodia to collectively drive cell-sheet movement. *J. Cell Sci.* 118:51–63.
8. Omelchenko, T., J. M. Vasiliev, …, E. M. Bonder. 2003. Rho-dependent formation of epithelial "leader" cells during wound healing. *Proc. Natl. Acad. Sci. USA.* 100:10788–10793.
9. Tamada, M., T. D. Perez, …, M. P. Sheetz. 2007. Two distinct modes of myosin assembly and dynamics during epithelial wound closure. *J. Cell Biol.* 176:27–33.
10. Bement, W. M., P. Forscher, and M. S. Mooseker. 1993. A novel cytoskeletal structure involved in purse string wound closure and cell polarity maintenance. *J. Cell Biol.* 121:565–578.
11. Brock, J., K. Midwinter, …, P. Martin. 1996. Healing of incisional wounds in the embryonic chick wing bud: characterization of the actin purse-string and demonstration of a requirement for Rho activation. *J. Cell Biol.* 135:1097–1107.
12. Anon, E., X. Serra-Picamal, …, B. Ladoux. 2012. Cell crawling mediates collective cell migration to close undamaged epithelial gaps. *Proc. Natl. Acad. Sci. USA.* 109:10891–10896.
13. Kiehart, D. P., C. G. Galbraith, …, R. A. Montague. 2000. Multiple forces contribute to cell sheet morphogenesis for dorsal closure in *Drosophila*. *J. Cell Biol.* 149:471–490.
14. Williams-Masson, E. M., A. N. Malik, and J. Hardin. 1997. An actin-mediated two-step mechanism is required for ventral enclosure of the *C. elegans* hypodermis. *Development.* 124:2889–2901.
15. Poujade, M., E. Grasland-Mongrain, …, P. Silberzan. 2007. Collective migration of an epithelial monolayer in response to a model wound. *Proc. Natl. Acad. Sci. USA.* 104:15988–15993.
16. Block, E. R., A. R. Matela, …, J. K. Klarlund. 2004. Wounding induces motility in sheets of corneal epithelial cells through loss of spatial constraints: role of heparin-binding epidermal growth factor-like growth factor signaling. *J. Biol. Chem.* 279:24307–24312.
17. Bellusci, S., G. Moens, …, J. Jouanneau. 1994. A scatter factor-like factor is produced by a metastatic variant of a rat bladder carcinoma cell line. *J. Cell Sci.* 107:1277–1287.
18. Reffay, M., L. Petitjean, …, P. Silberzan. 2011. Orientation and polarity in collectively migrating cell structures: statics and dynamics. *Biophys. J.* 100:2566–2575.
19. Hahn, W. C., C. M. Counter, …, R. A. Weinberg. 1999. Creation of human tumour cells with defined genetic elements. *Nature.* 400: 464–468.
20. Rasband, W. S. 1997–2012. ImageJ, http://imagej.nih.gov/ij/, U.S. National Institutes of Health, Bethesda, MD,
21. Bottema, M. 2000. Circularity of objects in images. *Proc. IEEE Int. Conf. Acoustics, Speech, Signal Proc.* 6:2247–2250, and vol. 4.
22. Landsberg, K. P., R. Farhadifar, …, C. Dahmann. 2009. Increased cell bond tension governs cell sorting at the *Drosophila* anteroposterior compartment boundary. *Curr. Biol.* 19:1950–1955.
23. Petitjean, L., M. Reffay, …, P. Silberzan. 2010. Velocity fields in a collectively migrating epithelium. *Biophys. J.* 98:1790–1800.
24. Gaush, C. R., W. L. Hard, and T. F. Smith. 1966. Characterization of an established line of canine kidney cells (MDCK). *Proc. Soc. Exp. Biol. Med.* 122:931–935.
25. Ayllón, V., and A. Rebollo. 2000. Ras-induced cellular events (review). *Mol. Membr. Biol.* 17:65–73.
26. Ridley, A. J. 2001. Rho GTPases and cell migration. *J. Cell Sci.* 114:2713–2722.
27. Deforet, M., M. C. Parrini, …, P. Silberzan. 2012. Automated velocity mapping of migrating cell populations (AVeMap). *Nat. Methods.* 9:1081–1083.

28. Puliafito, A., L. Hufnagel, …, B. I. Shraiman. 2012. Collective and single cell behavior in epithelial contact inhibition. *Proc. Natl. Acad. Sci. USA.* 109:739–744.

29. Arciero, J. C., Q. Mi, …, D. Swigon. 2011. Continuum model of collective cell migration in wound healing and colony expansion. *Biophys. J.* 100:535–543.

30. Almeida, L., P. Bagnerini, and A. Habbal. 2012. Modeling actin cable contraction. *Comput. Math. Appl.* 64:310–321.

31. Lee, P., and C. W. Wolgemuth. 2011. Crawling cells can close wounds without purse strings or signaling. *PLOS Comput. Biol.* 7:e1002007.

32. Bonnet, I., P. Marcq, …, F. Graner. 2012. Mechanical state, material properties and continuous description of an epithelial tissue. *J. R. Soc. Interface.* 9:2614–2623.

33. Chin, L., A. Tam, …, R. A. DePinho. 1999. Essential role for oncogenic Ras in tumour maintenance. *Nature.* 400:468–472.

34. Mali, P., D. Wirtz, and P. C. Searson. 2010. Interplay of RhoA and motility in the programmed spreading of daughter cells postmitosis. *Biophys. J.* 99:3526–3534.

35. Meadows, K. N., P. Bryant, …, K. M. Pumiglia. 2004. Activated Ras induces a proangiogenic phenotype in primary endothelial cells. *Oncogene.* 23:192–200.

36. Prass, M., K. Jacobson, …, M. Radmacher. 2006. Direct measurement of the lamellipodial protrusive force in a migrating cell. *J. Cell Biol.* 174:767–772.

37. Trepat, X.…, 2009. Physical forces during collective cell migration. *Nat. Phys.* 5:426–430.

38. Saez, A., E. Anon, …, B. Ladoux. 2010. Traction forces exerted by epithelial cell sheets. *J. Phys. Condens. Matter.* 22:194119.

39. Hall, A. 1998. Rho GTPases and the actin cytoskeleton. *Science.* 279:509–514.

40. Jaffe, A. B., and A. Hall. 2005. Rho GTPases: biochemistry and biology. *Annu. Rev. Cell Dev. Biol.* 21:247–269.

41. Etienne-Manneville, S., and A. Hall. 2002. Rho GTPases in cell biology. *Nature.* 420:629–635.

42. Rottner, K., A. Hall, and J. V. Small. 1999. Interplay between Rac and Rho in the control of substrate contact dynamics. *Curr. Biol.* 9:640–648.

43. Schallamach, A. 1963. A theory of dynamic rubber friction. *Wear.* 6:375–382.

44. Gerbal, F., P. Chaikin, …, J. Prost. 2000. An elastic analysis of *Listeria monocytogenes* propulsion. *Biophys. J.* 79:2259–2275.

45. Danen, E. H. J., J. van Rheenen, …, A. Sonnenberg. 2005. Integrins control motile strategy through a Rho-cofilin pathway. *J. Cell Biol.* 169:515–526.

46. Nobes, C. D., and A. Hall. 1999. Rho GTPases control polarity, protrusion, and adhesion during cell movement. *J. Cell Biol.* 144:1235–1244.

47. Ballestrem, C., B. Hinz, …, B. Wehrle-Haller. 2001. Marching at the front and dragging behind: differential alphaVβ3-integrin turnover regulates focal adhesion behavior. *J. Cell Biol.* 155:1319–1332.

48. Behrndt, M., G. Salbreux, …, C. P. Heisenberg. 2012. Forces driving epithelial spreading in zebrafish gastrulation. *Science.* 338:257–260.

49. Mayer, M., M. Depken, …, S. W. Grill. 2010. Anisotropies in cortical tension reveal the physical basis of polarizing cortical flows. *Nature.* 467:617–621.

50. Abreu-Blanco, M. T., J. M. Verboon, …, S. M. Parkhurst. 2012. Drosophila embryos close epithelial wounds using a combination of cellular protrusions and an actomyosin purse string. *J. Cell Sci.* 125:5984–5997.

Border forces and friction control epithelial closure dynamics
Supplementary Information

Olivier Cochet-Escartin, Jonas Ranft, Pascal Silberzan and Philippe Marcq

Physico-Chimie Curie, Institut Curie,

CNRS, Université Pierre et Marie Curie,

26 rue d'Ulm, F-75248 Paris Cedex 05 France

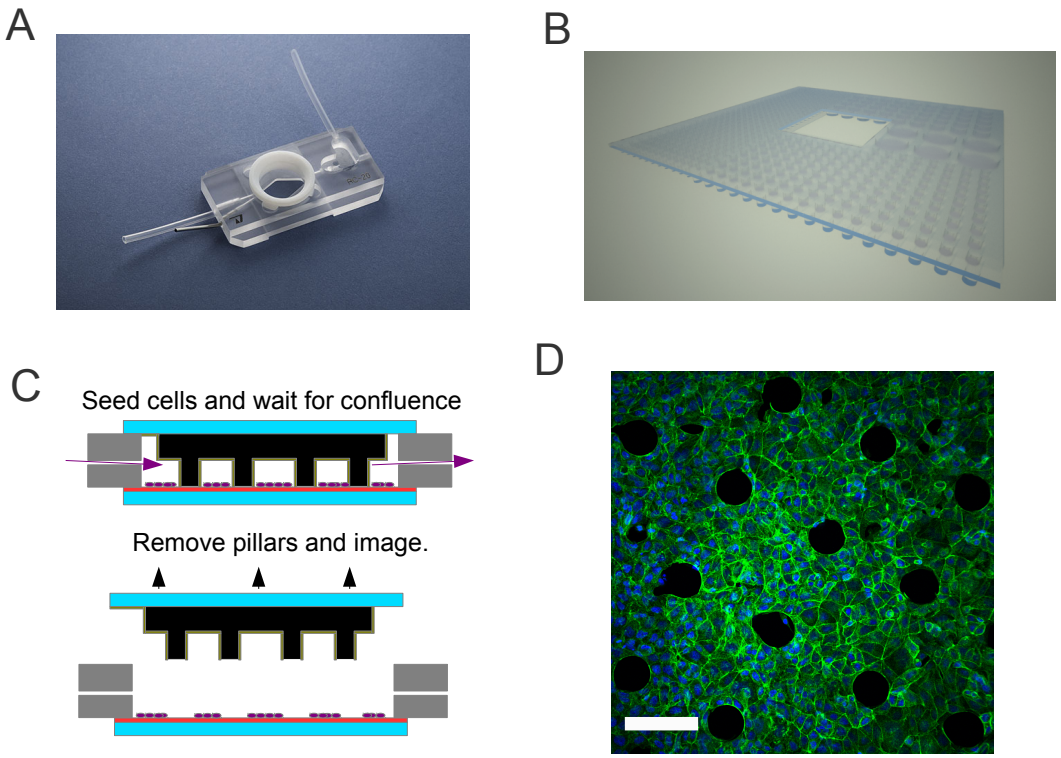

FIG. 1. **Experimental protocol and initial conditions.**

A: Picture of the flow chamber (Warner Instruments, model RC-20h).

B: Schematics of the PDMS template.

C: Schematics of the protocol. Cells are allowed to reach confluence before the template is removed.

D: MDCK wounds ($R_{\mathrm{w}} = 25\,\mu$m) were fixed while constrained under the template and labeled for F-actin (green) and nuclei (blue). Scale bar: $100\,\mu$m.

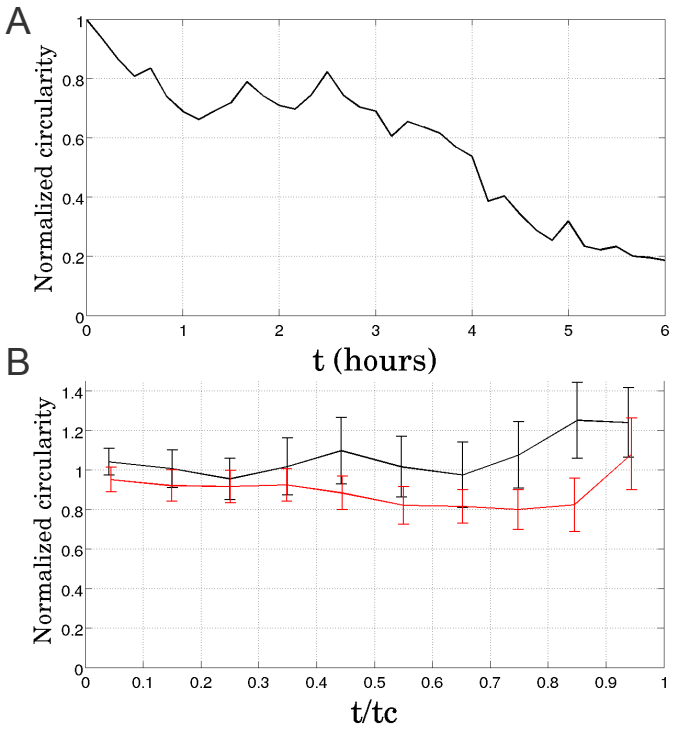

FIG. 2. **Circularity dynamics.**

A: Plot of the normalized circularity $c(t)/c(0)$ vs. time t of the large wound in Supplementary Movie 1 ($R_{\rm w} = 250\,\mu$m, red curve). The measurement stops when the fingers merge at $t = 6$h.

B: Plot of the normalized circularity $c(t)/c(0)$ vs. normalized time t/t_c, for the smallest ($R_{\rm w} = 25\,\mu$m, $N = 18$, black curve) and the largest initial radii ($R_{\rm w} = 100\,\mu$m, $N = 21$, red curve) of the small wounds. Error bars indicate the s.e.m.

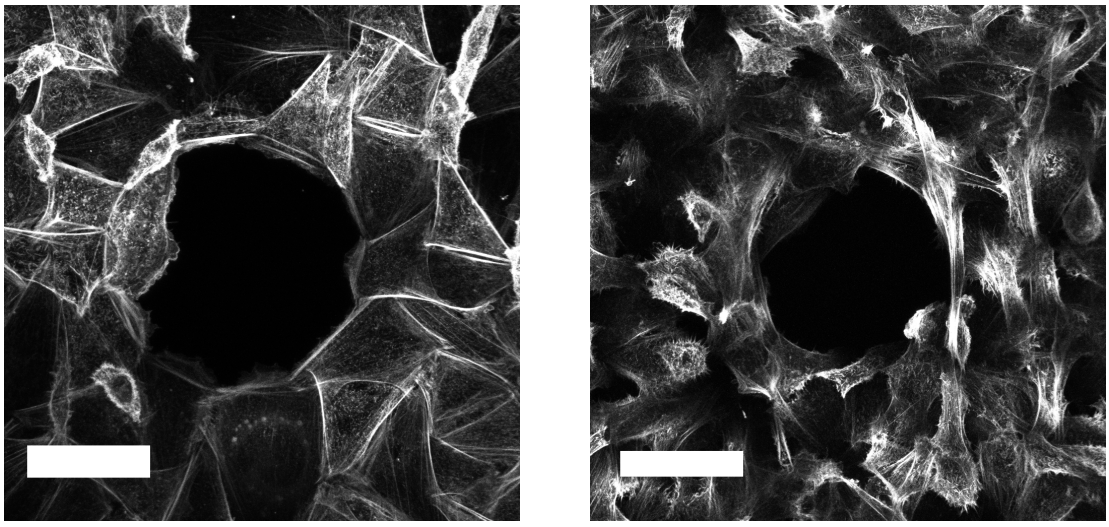

FIG. 3. **Actin staining on HEK cells.**

HEK-HT (left) and HEK-RasV12 (right) wounds ($R_{\mathrm{w}} = 50\,\mu$m) were allowed to close for 30 min and were then fixed and stained for F-actin with phalloidin. Numerous lamellipodia of different numbers and sizes are observed in both cases. Scale bar: $50\,\mu$m.

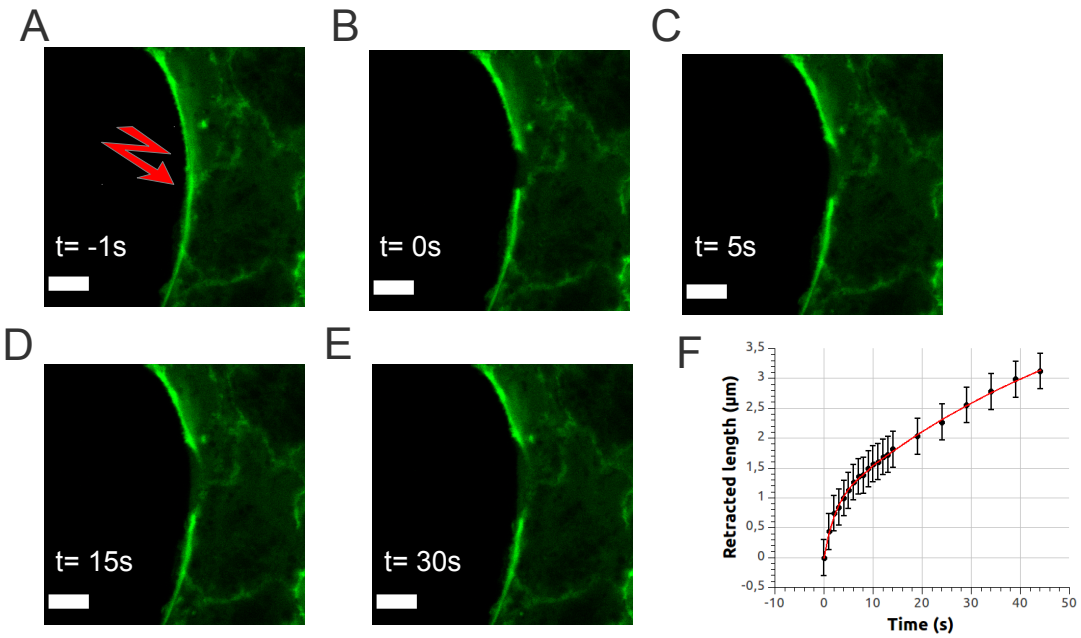

FIG. 4. **Local ablation of the acto-myosin cable.**

A-E: Timelapse of the retraction of an acto-myosin cable after laser ablation (MDCK-LifeAct-GFP wound, $R_w = 25\,\mu$m), imaged through confocal microscopy at $t = -1$ s, 0 s, 5 s, 15 s and 30 s. Here $t = 0$ s corresponds to the first image acquired immediately after ablation. Scale bar: $5\,\mu$m.

F: Retraction dynamics of one of the severed ends of the cable (black circles) with a double exponential fit (red curve) $\Delta l(t) = l_1\left(1 - e^{-t/\tau_2}\right) + l_2\left(1 - e^{-t/\tau_2}\right)$. The fit yields two characteristic times, $\tau_1 = 59.9 \pm 26.0$ s and $\tau_1 = 2.0 \pm 0.4$ s and two retraction lengths, $l_1 = 4.3 \pm 1.2\,\mu$m and $l_2 = 0.9 \pm 0.1\,\mu$m.

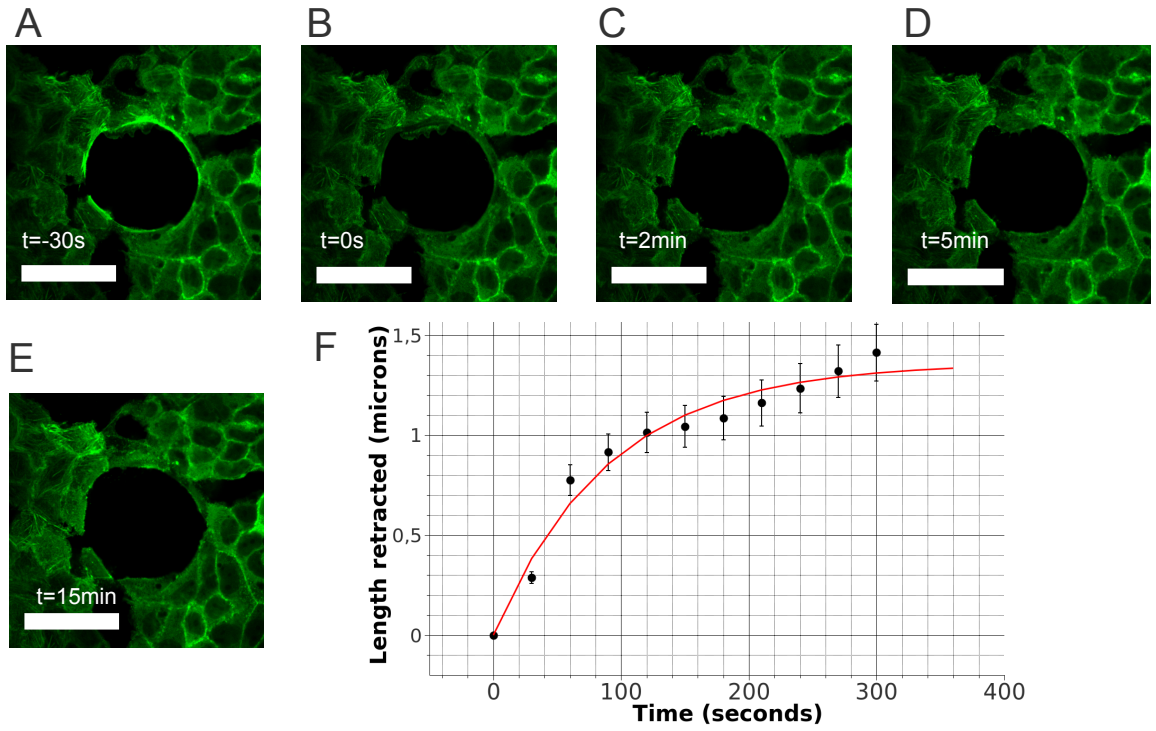

FIG. 5. **Ablation of the entire cable.**

A-E: Timelapse of the retraction of the wound edge after laser ablation of the circumferential cable (MDCK-LifeAct-GFP wound, $R_w = 25\,\mu$m), imaged through confocal microscopy at $t = -30$ s, 0 s, 2 min, 5 min and 15 min. Here $t = 0$ s corresponds to the first image acquired immediately after ablation. Scale bar: $50\,\mu$m. The actin cable was clearly apparent before ablation.

F: Plot of the retracted wound radius as a function of time (black circles), fitted by an exponentially decaying function of time $\Delta R(t) = l\left(1 - e^{-t/\tau}\right)$ (red curve). We obtain a retracted length of $l = 1.36 \pm 0.15\,\mu$m and a retraction time of $\tau = 90.7 \pm 27.9$ s.

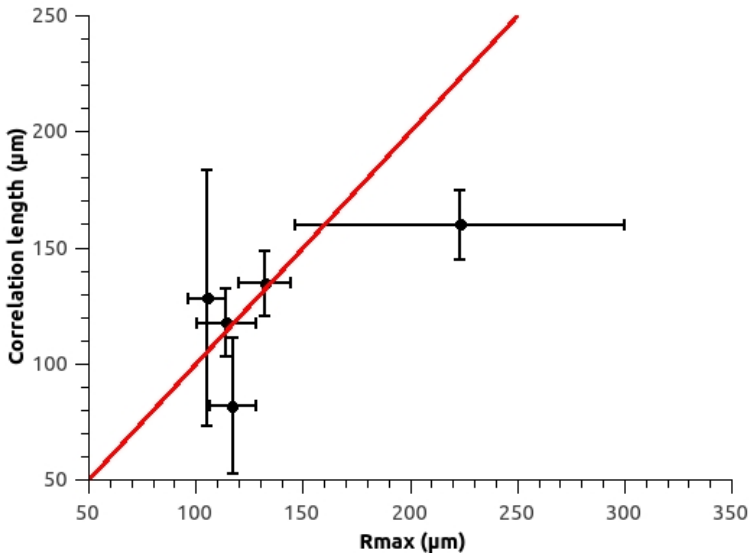

FIG. 6. **Velocity correlation length.**

Plot of the velocity correlation length vs. the cut-off radius $R_{\max}$ for all cell types and conditions. The red line is the first bissectrix, drawn to guide the eye. The cut-off radii and their error bars are obtained by fits of closure time data (see Fig. 5 and its caption). The correlation length is obtained from an exponential fit of the averaged velocity correlation function (see Methods), whose 95% confidence interval gives the error bars.

I. MODEL

We formulate a simple continuum mechanics description of wound closure, where we take advantage of our experimental observations that (i) cell division and death are negligible during the time of wound closure, (ii) there is no apparent orientational order of the cells, (iii) the wound shape remains approximately circular over the course of the experiment, and (iv) the flow is incompressible. We first detail our theoretical description (section I A), before we study three different epithelial rheologies, based on constitutive equations for either a simple inviscid or viscous liquid (sections I B and I C, respectively) or an elastic solid (section I D). Each rheology allows to obtain an analytical expression for the closure dynamics of the circular model wounds created by the experimental protocol.

A. Continuum mechanics epithelization

In order to understand wound closure dynamics on the scale of the epithelium, we aim at describing stresses and strains on large length scales, as compared to the cell size. Using continuum mechanics, we formulate an effective two-dimensional description of epithelization that takes into account the macroscopic tissue material properties.

Conservation of cell number in the epithelium is expressed by

$$\partial_t n + \partial_\alpha (n v_\alpha) = n(k_\mathrm{d} - k_\mathrm{a})\,, \tag{1}$$

where n is the cell number density, v_α the tissue velocity field, and k_d and k_a are the rates of cell division and cell death, respectively. By convention, greek indices denote vector components, and are summed when repeated. We assume $k_\mathrm{d} = k_\mathrm{a} = 0$ in the following, consistent with our experimental observations that both cell division and cell death are negligible during the time course of wound closure. Furthermore, the cell number density $n = n_0$ is approximately constant (Fig. 3E-F). The cell number balance equation then becomes a constraint on the tissue flow field, $\partial_\alpha v_\alpha = 0$: the flow is incompressible (Fig. 3B).

In a continuous material, mechanical forces are balanced locally if inertial terms can be neglected, as is the case here. Force balance is then expressed as

$$\partial_\beta \sigma_{\alpha\beta} = -f_\alpha^\mathrm{ext}\,, \tag{2}$$

where internal forces are described by the stress tensor $\sigma_{\alpha\beta}$, and $f_\alpha^{\rm ext}$ denotes external forces. Here, the external force is due to friction with the substrate, and with ξ being a friction coefficient we write $f_\alpha^{\rm ext} = -\xi v_\alpha$. Together with a constitutive equation for the stress tensor and appropriate boundary conditions, Eq. (2) allows to solve for the deformation and cell flow field in the epithelium. The constitutive equation for the stress tensor accounts for the tissue material properties. In general, the stress tensor can be decomposed into an isotropic part σ and a deviatoric (traceless) part $\tilde{\sigma}_{\alpha\beta}$ according to

$$\sigma_{\alpha\beta} = \sigma\delta_{\alpha\beta} + \tilde{\sigma}_{\alpha\beta}\,, \tag{3}$$

where $\delta_{\alpha\beta}$ denotes Kronecker's symbol, and $\tilde{\sigma}_{\alpha\alpha} = 0$ by definition.

In the following, we consider an epithelium where a model wound with initial radius R_0 is created at $t_0 = 0$, centered about the origin O. We assume that the circular shape is preserved during the closure process and denote by $R(t)$ the wound radius at time t (Fig. 4A). The wound closes because of forces exerted at the margin, either by actively pulling cells or by an acto-myosin cable that spans over the whole perimeter. Using polar coordinates, the stress boundary condition at the margin reads

$$\sigma_{rr}|_{R(t)} = \sigma_{\rm p} + \frac{\gamma}{R}\,, \tag{4}$$

where $\sigma_{\rm p}$ is a protrusive stress that accounts for forces exerted by the cells at the wound margin, and γ is a tension that describes purse-string forces due to an acto-myosin cable around the wound. Introducing the length scale $R_\gamma = \gamma/\sigma_{\rm p}$, we expect that the purse-string mechanism (resp. the protrusive forces) will dominate the dynamics at scales smaller (resp. larger) than R_γ.

Assuming rotational invariance of the flow allows to express the velocity field as $\vec{v} = v_r(r,t)\,\vec{e}_r$, where the non-vanishing radial component depends only on the distance r relative to the center O of the initial wound. Using the incompressibility constraint $\nabla\cdot\vec{v} = 0$, we obtain $v_r(r,t) = A(t)/r$, where $A(t)$ can be determined from the kinematic boundary condition at the margin. Since $v_r(r = R(t), t) = \dot{R}(t)$, we can express $v_r(r,t)$ in terms of r and the wound radius $R(t)$ only

$$v_r(r,t) = \frac{R(t)\dot{R}(t)}{r}\,. \tag{5}$$

Using this expression with Eqs. (2) and (4) allows to find a dynamical equation for the wound radius $R(t)$. In the following sections, we derive and solve this dynamical equation—

or rather the inverse problem t = t(R)—for three different constitutive equations, each highlighting a different epithelial rheology.

B. Inviscid fluid

For simplicity, we first assume that the epithelium behaves as an incompressible, inviscid fluid on the relevant time and length scales. In this case, the stresses are purely isotropic and do not depend on tissue viscosity or elasticity. In the incompressible limit, the isotropic part of the stress becomes a Lagrange multiplier which is determined from the mechanical boundary conditions, and we simply write $\sigma = -P$. The stress tensor thus reads

$$\sigma_{\alpha\beta} = -P\,\delta_{\alpha\beta}\,, \tag{6}$$

where P is the pressure field at the scale of the epithelium. Using rotational invariance ($P = P(r,t)$) and Eq. (5) for the velocity field, the force balance (2) becomes $\partial_r P = -\xi R\dot{R}/r$. The pressure follows as $P = -\xi R\dot{R}\ln r + C$, where $C = C(t)$ is a function of time. Note that in principle, $C(t)$ is determined by the boundary condition at $r \to \infty$, which is an ill-defined limit in two dimensions. We therefore introduce a constant, long-range cut-off $R_{\max}$ at which the pressure vanishes and write

$$P(r,t) = -\xi R(t)\dot{R}(t)\ln\frac{r}{R_{\max}}\,. \tag{7}$$

Since $\dot{R}(t) \le 0$ and $r \le R_{\max}$, the pressure is negative: the epithelium is under tension.

A dynamical equation for the wound radius $R(t)$ follows from the stress boundary condition at the margin, Eq. (4), and with the above expression for P we find

$$\xi R\ln\left(\frac{R}{R_{\max}}\right)\dot{R} = \sigma_{\rm p} + \frac{\gamma}{R}\,. \tag{8}$$

Using the characteristic length $R_\gamma = \gamma/\sigma_{\rm p}$, we rewrite the evolution equation as

$$\mathrm{d}t = \frac{\xi}{\sigma_{\rm p}}\,\frac{R^2}{R+R_\gamma}\ln\left(\frac{R}{R_{\max}}\right)\mathrm{d}R\,. \tag{9}$$

Integration yields the function $t(R) = \tilde{t}(R) - \tilde{t}(R_0)$, with

$$\begin{aligned} 4D\,\tilde{t}(R) = -R^2\,&\left(1 + 2\ln\frac{R_{\max}}{R}\right) \\ &+\,4R_\gamma R\left(1+\ln\frac{R_{\max}}{R}\right) + 4R_\gamma^2\left(\mathrm{Li}_2(-\frac{R}{R_\gamma}) - \ln\frac{R_{\max}}{R}\ln\frac{R+R_\gamma}{R_\gamma}\right)\,. \end{aligned} \tag{10}$$

Here, we introduce the epithelization coefficient $D = \sigma_\mathrm{p}/\xi$, which has the dimension of a diffusion coefficient, and Li_2 stands for the dilogarithm function defined as $\mathrm{Li}_2(x) = \sum_{k=1}^{\infty} x^k/k^2$. The integration constant is determined by the initial condition $t(R_0) = 0$. Since $\mathrm{Li}_2(0) = 0$, the closure time is finite: $t_\mathrm{c} \equiv t(R=0) = \tilde{t}(0) - \tilde{t}(R_0) = -\tilde{t}(R_0)$.

When the contribution of the acto-myosin cable is negligible, $R_\gamma \to 0$, the expression for $t(R)$ simplifies to

$$t(R) \simeq \frac{R_0^2}{4D}\left(1 + 2\ln\frac{R_\mathrm{max}}{R_0}\right) - \frac{R^2}{4D}\left(1 + 2\ln\frac{R_\mathrm{max}}{R}\right), \tag{11}$$

and the closure time follows as

$$t_\mathrm{c}(R_0) \simeq \frac{R_0^2}{4D}\left(1 + 2\ln\frac{R_\mathrm{max}}{R_0}\right) \tag{12}$$

in the same limit. This result implies that under the above assumptions, *i.e.*, for an inviscid epithelium, the closure of a circular model wound completes in a finite time, independently of whether a contractile cable contributes to force production or not.

C. Viscous fluid

Taking into account viscous stresses, the deviatoric stress tensor is given by

$$\tilde{\sigma}_{\alpha\beta} = 2\eta\tilde{v}_{\alpha\beta}\,, \tag{13}$$

where η is an effective tissue shear viscosity and $\tilde{v}_{\alpha\beta}$ is the traceless part of the velocity gradient tensor $v_{\alpha\beta} = \frac{1}{2}(\partial_\alpha v_\beta + \partial_\beta v_\alpha)$. The isotropic part of the stress becomes again a Lagrange multiplier, and we write $\sigma = -P$ as before. Incompressibility also implies that $v_{\gamma\gamma} = 0$, and thus $\tilde{v}_{\alpha\beta} = v_{\alpha\beta}$.

Taking into account rotational invariance, the radial component of the force balance (2) reads

$$\partial_r\sigma + \partial_r\tilde{\sigma}_{rr} + 2\frac{\tilde{\sigma}_{rr}}{r} = \xi v_r\,. \tag{14}$$

Inserting the constitutive equations, we obtain as before $\partial_r P = -\xi R\dot{R}/r$. Expression (7) for the pressure field is therefore unchanged. With $\sigma_{rr} = -P + 2\eta\,\partial_r v_r$, the boundary condition (4) now leads to

$$\dot{R} = \frac{\gamma + \sigma_\mathrm{p} R}{\xi R^2 \ln R/R_\mathrm{max} - 2\eta}\,. \tag{15}$$

Introducing the length scale $R_\eta = \sqrt{\eta/\xi}$, integration yields

$$t(R) = \tilde{t}(R) - \tilde{t}(R_0)\,, \tag{16}$$

with

$$\begin{aligned} 4D\,\tilde{t}(R) = &-R^2\left(1 + 2\ln\frac{R_{\max}}{R}\right) + 8R_\eta^2\,\ln\frac{R_{\max}}{R+R_\gamma} \\ &+ 4R_\gamma R\left(1 + \ln\frac{R_{\max}}{R}\right) + 4R_\gamma^2\left(\mathrm{Li}_2(-\frac{R}{R_\gamma}) - \ln\frac{R_{\max}}{R}\ln\frac{R+R_\gamma}{R_\gamma}\right)\,. \end{aligned} \tag{17}$$

In the limit of vanishing viscosity, $R_\eta \to 0$, the above expression reduces to Eq. (10), consistent with the assumption of vanishing deviatoric stresses in the inviscid case.

The closure time is again finite, $t_\mathrm{c} \equiv t(R=0) = \tilde{t}(0) - \tilde{t}(R_0) = 2(\eta/\sigma_\mathrm{p})\,\ln(R_{\max}/R_\gamma) - \tilde{t}(R_0)$, and tends to expression (12) in the limit where both R_η and R_γ are negligible. However, if R_η remains finite, the closure time diverges in the limit $R_\gamma \to 0$. The model predicts that, in the absence of a contractile cable, circular model wounds do not complete closure in finite time when viscous stresses in the epithelium cannot be neglected. This somewhat surprising result is an artifact of the continuous description: in fact closure will complete, thanks to cell-scale mechanisms not taken into account by the model, as soon the wound radius is smaller than a microscopic cut-off length a, with a finite closure time of the order of $\tilde{t}(a) - \tilde{t}(R_0)$.

D. Elastic solid

When deformations are small, the constitutive equation for an incompressible elastic material reads

$$\tilde{\sigma}_{\alpha\beta} = 2\mu\tilde{u}_{\alpha\beta}\,, \tag{18}$$

where μ is the shear elastic modulus and $\tilde{u}_{\alpha\beta}$ is the traceless part of the strain tensor. The latter is defined as $u_{\alpha\beta} = \frac{1}{2}(\partial_\alpha u_\beta + \partial_\beta u_\alpha)$ for a displacement field u_α. Incompressibility implies that $u_{\gamma\gamma} = 0$, and thus $\tilde{u}_{\alpha\beta} = u_{\alpha\beta}$. In this limit, the isotropic stress becomes again a Lagrange multiplier and we write $\sigma = -P$.

In the case of rotational invariance, we can express the elastic displacement field as $\vec{u} = u_r(r,t)\,\vec{e}_r$. Using the incompressibility condition $\nabla\cdot\vec{u} = 0$ together with the boundary condition $u_r(R,t) = R(t) - R_0$, we obtain u_r as a function of r and $R(t)$,

$$u_r(r,t) = \frac{R(t)(R(t)-R_0)}{r}\,. \tag{19}$$

One can check that this expression verifies $\dot{R}(t) \equiv (\partial_t + v_r\partial_r)\, u_r(r = R(t), t) = v_r(r = R(t), t)$ at all times $t \geq 0$. The differential equation for P resulting from force balance is again unchanged, P is given by Eq. (7). Since the radial stress in the epithelium is given by

$$\sigma_{rr} = -P + 2\mu\partial_r u_r\,, \tag{20}$$

the stress boundary condition (4) yields the following dynamical equation for the wound radius $R(t)$

$$\dot{R} = \frac{\gamma + \sigma_{\rm p} R + 2\mu(R - R_0)}{\xi R^2 \ln R/R_{\rm max}}\,. \tag{21}$$

Formally, elastic restoring forces and forces driving epithelization balance at the equilibrium radius $R_{\rm e}$ with

$$R_{\rm e} = \frac{2\mu R_0 - \gamma}{\sigma_{\rm p} + 2\mu}\,. \tag{22}$$

Taking into account the initial condition $t(R_0) = 0$, integration of Eq. (21) yields

$$t(R) = \tilde{t}(R) - \tilde{t}(R_0)\,, \tag{23}$$

where $\tilde{t}(R)$ is given by

$$4D_S\,\tilde{t}(R) = -R^2 - 4RR_{\rm e} + 2R\,(R + 2R_{\rm e})\ln\frac{R}{R_{\rm max}} + 4R_{\rm e}^2\left(\ln\frac{R}{R_{\rm max}}\ln\left(1 - \frac{R}{R_{\rm e}}\right) + {\rm Li}_2\left(\frac{R}{R_{\rm e}}\right)\right)\,. \tag{24}$$

Here, $D_{\rm S} = \frac{\sigma_{\rm p}+2\mu}{\xi}$ has the dimension of a diffusion coefficient, and differs from the epithelization coefficient D by a factor of $(1 + \frac{2\mu}{\sigma_{\rm p}})$. In the limit of vanishing elastic modulus ($2\mu \ll \sigma_{\rm p}$ and $2\mu \ll \gamma/R_0$), expression (24) for $t(R)$ reduces to the one obtained for an inviscid fluid as given by Eq. (10). Of course only positive values of the radius are physical and closure stops when $R(t_c) = 0$.

The above result for $t(R)$ implies that the wound closure eventually completes whenever $R_{\rm e} \leq 0$. This is the case for large enough values of the line tension γ, *i.e.*, $\gamma \geq 2\mu R_0$. The closure time is then given by $t_{\rm c} = t(R = 0) = \tilde{t}(0) - \tilde{t}(R_0) = -\tilde{t}(R_0)$. In the particular case where line tension and elasticity balance exactly, $\gamma = 2\mu R_0$ and thus $R_{\rm e} = 0$, Eq. (24) reduces to Eq. (11), and the closure time follows as given by Eq. (12) with the substitution $D \to D_S$.

When the equilibrium radius is positive but small, $0 < R_{\rm e} \simeq a$, where a is of the order of the size of a cell, epithelization may proceed to a scale small enough that microscopic

mechanisms, not accounted for within the continuous description, terminate the epithelization process. This might be the case even for small values of the line tension $0 \leq \gamma \leq 2\mu R_0$ provided that the protrusive stress dominates the elastic modulus, $\sigma_\mathrm{p} \gg 2\mu$ (see Eq. (22)).

When the epithelial elastic modulus is large enough ($2\mu \sim \sigma_\mathrm{p}$ and $2\mu > \gamma/R_0$), the equilibrium radius is strictly positive: wound closure halts due to elastic forces. Expression (24) takes complex values when $R_\mathrm{e} > 0$. However, the identity

$$\mathrm{Li}_2(x) + \mathrm{Li}_2(1-x) + \ln(1-x)\ln x = \frac{\pi^2}{6} \tag{25}$$

allows to rewrite $t(R)$ as

$$t(R) = \frac{\xi}{4\,(\sigma_\mathrm{p}+2\mu)}\left[(R_0^2-R^2) + 4(R_0-R)R_\mathrm{e} + 2R\,(R+2R_\mathrm{e})\ln\frac{R}{R_\mathrm{max}}\right.$$
$$\left. - 2R_0\,(R_0+2R_\mathrm{e})\ln\frac{R_0}{R_\mathrm{max}} + 4R_\mathrm{e}^2\left(\mathrm{Li}_2(1-\frac{R_0}{R_\mathrm{e}}) - \mathrm{Li}_2(1-\frac{R}{R_\mathrm{e}}) + \ln\frac{R-R_\mathrm{e}}{R_0-R_\mathrm{e}}\ln\frac{R_\mathrm{e}}{R_\mathrm{max}}\right)\right], \tag{26}$$

where all terms are real-valued for $R > R_\mathrm{e} > 0$. In this case the closure time is infinite.

II. DATA ANALYSIS

In section I, we obtained analytical expressions of $t_\mathrm{c}(R_0)$ and $t(R)$, corresponding to different epithelial rheologies. In order to estimate the physical parameters of the epithelia, we now fit experimental data by these expressions, using the Levenberg-Marquardt algorithm for nonlinear least-squares fitting, implemented in PYTHON (LMFIT package, `http://pypi.python.org/pypi/lmfit/`, Least-Squares Minimization with Bounds and Constraints). We successively examine fits of closure times vs. initial effective radii in section II A and fits of individual trajectories $R(t)$ in section II B.

A. Closure time data

The closure time is a robust quantity that depends only weakly on the image analysis method: at a given time t, the wound is either open or closed. The experimental uncertainty on t_c is of the order of the time resolution of data acquisition, between 3 and 15 minutes depending on the size of the wound. Fig. 7 gives the empirical cumulative distribution functions of closure times for MDCK wounds, including the effect of inhibitors. Fig. 8

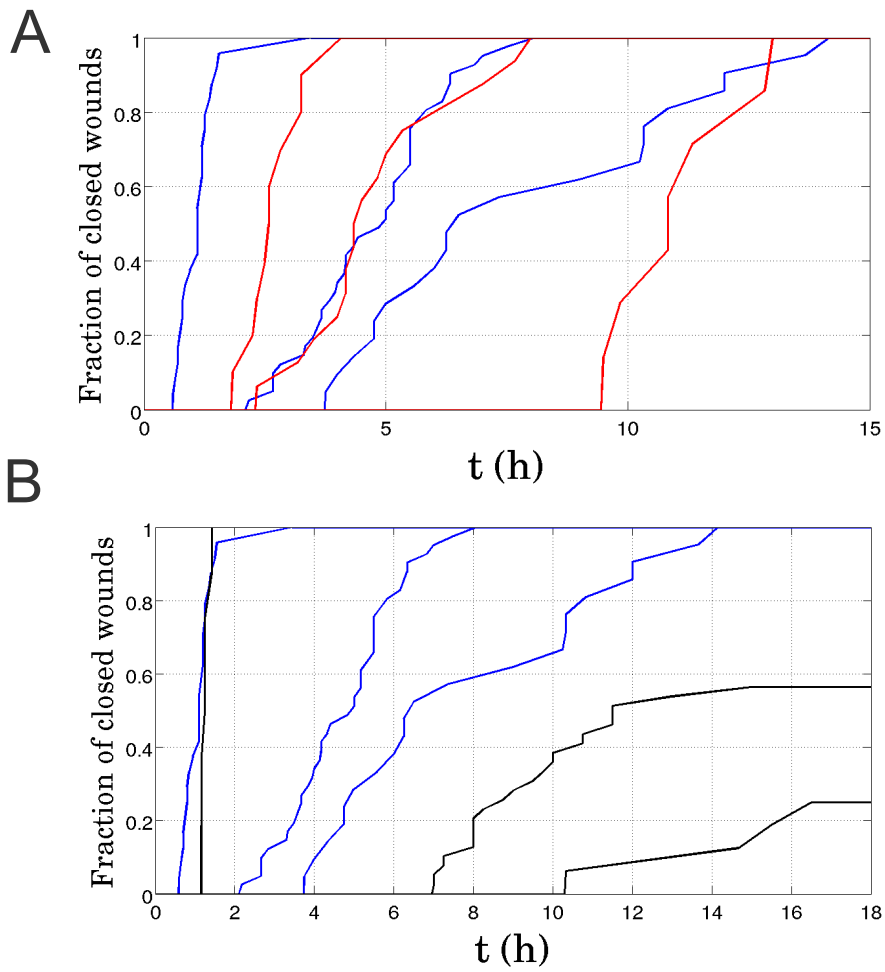

FIG. 7. **Cumulative distributions of closure times for MDCK wounds.**

A: comparison between wild-type (blue curves, $N = 24$, 41 and 16 respectively) and Rho$^-$ assays (red curves, $N = 10$, 16 and 7 respectively), $R_\mathrm{w} = 25\,\mu$m, $50\,\mu$m and $100\,\mu$m from left to right.

B: comparison between wild-type (blue curves, same data as in A) and Rac$^-$ assays (red curves, $N = 8$, 39 and 16 respectively), same sizes from left to right. A fraction of the Rac$^-$ wounds do not complete closure within the observation time $t = 18$ h.

shows that closure time data pertaining to all cell types and conditions is well fitted by Equation (12), obtained for an inviscid epithelium without cable.

We now ask whether this simple description is robust, and consider this question in the case of MDCK wild-type wounds, for which the number of wounds is largest ($N = 130$). As shown in section I, different assumptions made on the epithelial rheology lead to different expressions of the closure time t_c as a function of the initial radius R_0. Although an

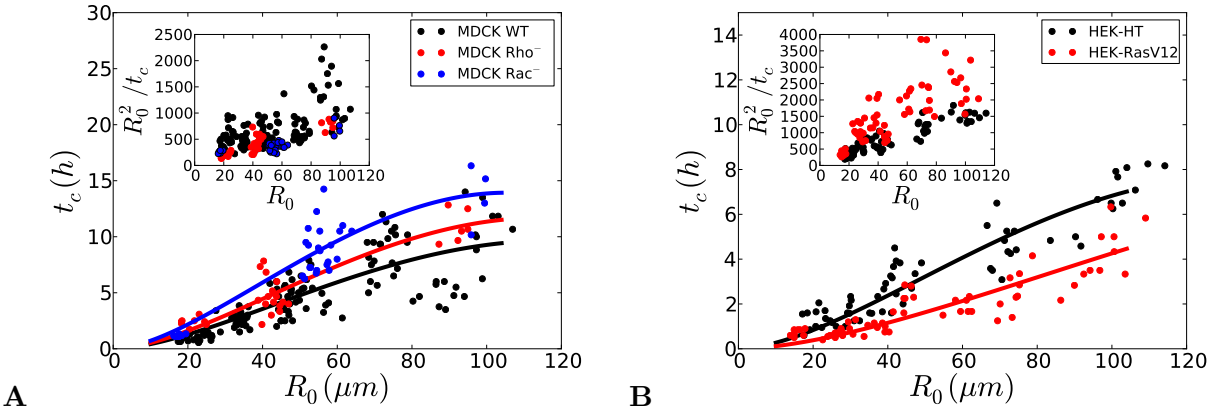

FIG. 8. **Inviscid fluid:** Closure time t_c as a function of the initial effective radius R_0 (circles), fitted by Equation (27) (solid curves) with the constraints $D, R_{\max} \geq 0$. One dot corresponds to one wound.

A: MDCK wounds. Wild Type, Rho$^-$ and Rac$^-$ assays. The physical parameters of epithelization $(D, R_{\max})$ are given within a 95 % confidence interval. MDCK WT ($N = 130$): $\sigma_p/\xi = 353 \pm 38\,\mu m^2\,h^{-1}$, $R_{\max} = 117 \pm 11\,\mu m$; MDCK Rho$^-$ ($N = 30$): $\sigma_p/\xi = 278 \pm 40\,\mu m^2\,h^{-1}$, $R_{\max} = 114 \pm 14\,\mu m$; MDCK Rac$^-$ ($N = 34$): $\sigma_p/\xi = 198 \pm 22\,\mu m^2\,h^{-1}$, $R_{\max} = 105 \pm 9\,\mu m$;

B: HEK-HT and HEK-RasV12 wounds. HEK-HT ($N = 63$): $\sigma_p/\xi = 572 \pm 57\,\mu m^2\,h^{-1}$, $R_{\max} = 132 \pm 12\,\mu m$; HEK-RasV12 ($N = 65$): $\sigma_p/\xi = 1531 \pm 363\,\mu m^2\,h^{-1}$, $R_{\max} = 223 \pm 77\,\mu m$.

Insets: for all cell types and conditions, the ratio of initial effective area over closure time R_0^2/t_c increases with initial radius R_0.

inviscid epithelium may close without cable, strictly speaking, both a viscous and an elastic epithelium require a finite line tension ($\gamma \neq 0$) for closure to reach completion.

For convenience, we summarize below the analytical expressions obtained for $t_c(R_0)$:

- *inviscid liquid, without cable* ($\gamma = 0$, $D = \sigma_p/\xi$):

$$4D\,t_c(R_0) = R_0^2\left(1 + 2\ln\frac{R_{\max}}{R_0}\right) \tag{27}$$

- *inviscid liquid, with cable* ($\gamma \neq 0$, $R_\gamma = \gamma/\sigma_p$):

$$4D\,t_c(R_0) = R_0^2\left(1 + 2\ln\frac{R_{\max}}{R_0}\right) - 4R_0R_\gamma\left(1 + \ln\frac{R_{\max}}{R_0}\right) - 4R_\gamma^2\left(\mathrm{Li}_2(-\frac{R_0}{R_\gamma}) + \ln\frac{R_{\max}}{R_0}\ln\frac{R_\gamma}{R_0 + R_\gamma}\right) \tag{28}$$

- *viscous liquid, with cable* ($R_\eta = \sqrt{\eta/\xi}$):

$$4D\,t_{\rm c}(R_0) = R_0^2\left(1+2\ln\frac{R_{\rm max}}{R_0}\right) - 4R_0R_\gamma\left(1+\ln\frac{R_{\rm max}}{R_0}\right) + 8R_\eta^2\,\ln\frac{R+R_\gamma}{R_\gamma} - 4R_\gamma^2\left(\mathrm{Li}_2(-\frac{R_0}{R_\gamma}) + \ln\frac{R_{\rm max}}{R_0}\ln\frac{R_\gamma}{R_0+R_\gamma}\right) \quad (29)$$

- *elastic solid, with cable* ($R_{\rm e} = \frac{2\mu R_0-\gamma}{\sigma_{\rm p}+2\mu} \leq 0$, $D_S = \frac{\sigma_{\rm p}+2\mu}{\xi}$):

$$4D_S\,t_{\rm c}(R_0) = R_0^2\left(1+2\ln\frac{R_{\rm max}}{R_0}\right) + 4R_0R_{\rm e}\left(1+\ln\frac{R_{\rm max}}{R_0}\right) - 4R_{\rm e}^2\left(\mathrm{Li}_2(\frac{R_0}{R_{\rm e}}) - \ln\frac{R_{\rm max}}{R_0}\ln(1-\frac{R_0}{R_{\rm e}})\right) \quad (30)$$

First, we investigate whether cable tension may significantly contribute to force production at the margin (Fig. 9A). Fitting closure time data with expression (28), obtained for an inviscid epithelium with a cable, we find that:

- values of D and $R_{\rm max}$ are consistent within error bars with those obtained without a cable;

- the length scale $R_\gamma = 7 \pm 11\,\mu$m is small compared to R_0 ($R_\gamma \ll R_0$), as well as to the wound radius ($R_\gamma \ll R(t)$) except in the late stages of closure.

When the epithelium is modeled as an inviscid fluid, we conclude that the contribution of the actomyosin cable to the stress boundary condition is negligible. For the sake of completeness, we investigate the case where protrusive forces are small compared to the cable tension ($R_\gamma \gg R_0$). In this case, the closure time is given by

$$9\frac{\gamma}{\xi}\,t_{\rm c}(R_0) = R_0^3\left(1+3\ln\frac{R_{\rm max}}{R_0}\right), \quad (31)$$

which follows from integration of Eq. (8) with $\sigma_{\rm p} = 0$. This expression fits the closure time data rather poorly (Fig. 9A): in particular the value obtained for $R_{\rm max}$ is inconsistent with the sizes considered. We conclude that protrusive forces at the margin cannot be neglected.

Second, we ask whether neglecting viscous stresses in the epithelium is legitimate, and fit data with Eq. (29) (see Fig. 9B). We obtain:

- values of D and $R_{\rm max}$ consistent within error bars with those found in the inviscid case without a cable;

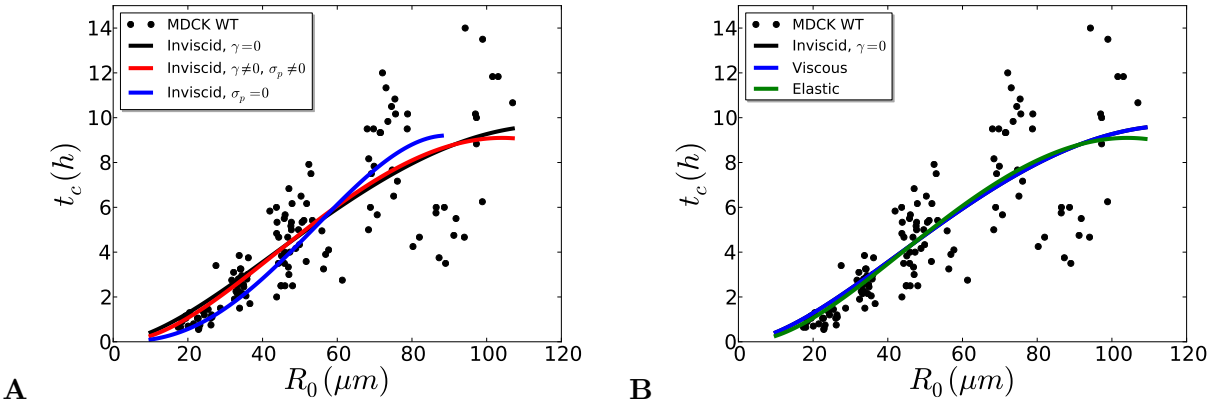

FIG. 9. **Model selection:** MDCK wild type wounds.

A Border forces. The closure time t_c is plotted as a function of the initial effective radius R_0 (black circles), and fitted by analytical expressions obtained when the epithelium is modeled as an inviscid fluid:

- Equation (27): black line, $\sigma_p \neq 0, \gamma = 0$, constraints $D, R_{max} \geq 0$, fitted parameter values $\sigma_p/\xi = 353 \pm 38\,\mu m^2\,h^{-1}$, $R_{max} = 117 \pm 11\,\mu m$;

- Equation (28): red line, $\sigma_p \neq 0, \gamma \neq 0$, constraints $D, R_{max}, R_\gamma \geq 0$, fitted parameter values $\sigma_p/\xi = 247 \pm 108\,\mu m^2\,h^{-1}$, $R_{max} = 104 \pm 13\,\mu m$, $R_\gamma = 7 \pm 11\,\mu m$;

- Equation (31): blue line , $\sigma_p = 0, \gamma \neq 0$, constraints $\gamma/\xi, R_{max} \geq 0$, fitted parameter values $\gamma/\xi = 8592 \pm 606\,\mu m^3\,h^{-1}$, $R_{max} = 89 \pm 2\,\mu m$.

B Tissue rheology. The closure time t_c is plotted as a function of the initial effective radius R_0 (black circles), and fitted by analytical expressions obtained when both lamellipodial protrusions and an actomyosin cable are taken into account ($\sigma_p \neq 0, \gamma \neq 0$):

- Equation (27): black line, inviscid fluid as in A;

- Equation (29): blue line, viscous fluid, constraints $D, R_{max}, R_\gamma, R_\eta \geq 0$, the (blue) fitted curve cannot be distinguished from the black curve, with identical parameter values of D and R_{max}, and $R_\gamma = R_\eta = 0$.

- Equation (30): green line, elastic solid, constraints $D, R_{max}, \mu, \gamma \geq 0$, the fit yields $\sigma_p/\xi \approx 247\,\mu m^2\,h^{-1}$, $R_{max} = 104\,\mu m$, $\frac{2\mu}{\sigma_p} = 0$, $R_\gamma \approx 7\,\mu m$, from which we deduce $R_e = -R_\gamma < 0$.

  - a length scale $R_\gamma = 7 \pm 51\,\mu m$, consistent with a zero value;

  - a viscous length scale $R_\eta = 0.01 \pm 8000\,\mu m$, consistent with a zero value.

We conclude that the actomyosin cable can be neglected in this case as well ($R_\gamma \ll R_0$), and that dissipation is dominated by friction with the substrate ($R_\eta \ll R_0$): epithelial viscosity can be neglected.

Finally, we study closure time data taking into account elastic stresses, and fit data with Equation (30), constraining the parameters D_s, $R_{\max}$, $2\mu/\sigma_{\mathrm{p}}$, and R_γ to be positive. The fitted value of $2\mu/\sigma_{\mathrm{p}}$ is consistent with zero: elastic forces are vanishingly small when compared to protrusive forces. In addition, the fitted values of $D_s = D$, $R_{\max}$ and R_γ are consistent with those obtained for an inviscid fluid when the cable line tension is taken into account. In this case, Equation (30) reduces to Equation (28).

Altogether, we find that the model of the monolayer as an inviscid fluid describes wild-type MDCK data satisfactorily, and that viscous and elastic contributions to the stress are negligibly small. Furthermore, the contribution of the cable to force production is small compared to that of lamellipodia. We hypothesize that the main function of the contractile circumferential cable is to stabilize the free epithelial boundary. Since $R_\gamma \ll R_0$ in all cases considered, we neglect cable tension in the following and set $\gamma = 0$ unless explicitly specified otherwise.

B. Closure trajectories

In sections II B 1 and II B 2, we examine the individual trajectories of closing and non-closing wounds.

1. Closing wounds

For brevity, we focus on MDCK-WT and HEK-HT wounds, and fit Equation (11) to data, using for convenience time as a function of radius $t(R)$. In Section II A, we showed that the simplest model of the monolayer as an inviscid fluid driven by cell protrusions at the margin suffices to describe closure time data. We therefore fit trajectories using the same model (see Fig. 10A), obtain one set of physical parameters per wound, and check the consistency of our results.

Since $R_{\max}$ was previously found to vary little, we constrain $R_{\max}$ to belong to the 95% confidence interval obtained from closure time data (see the caption of Fig. 8 for numerical

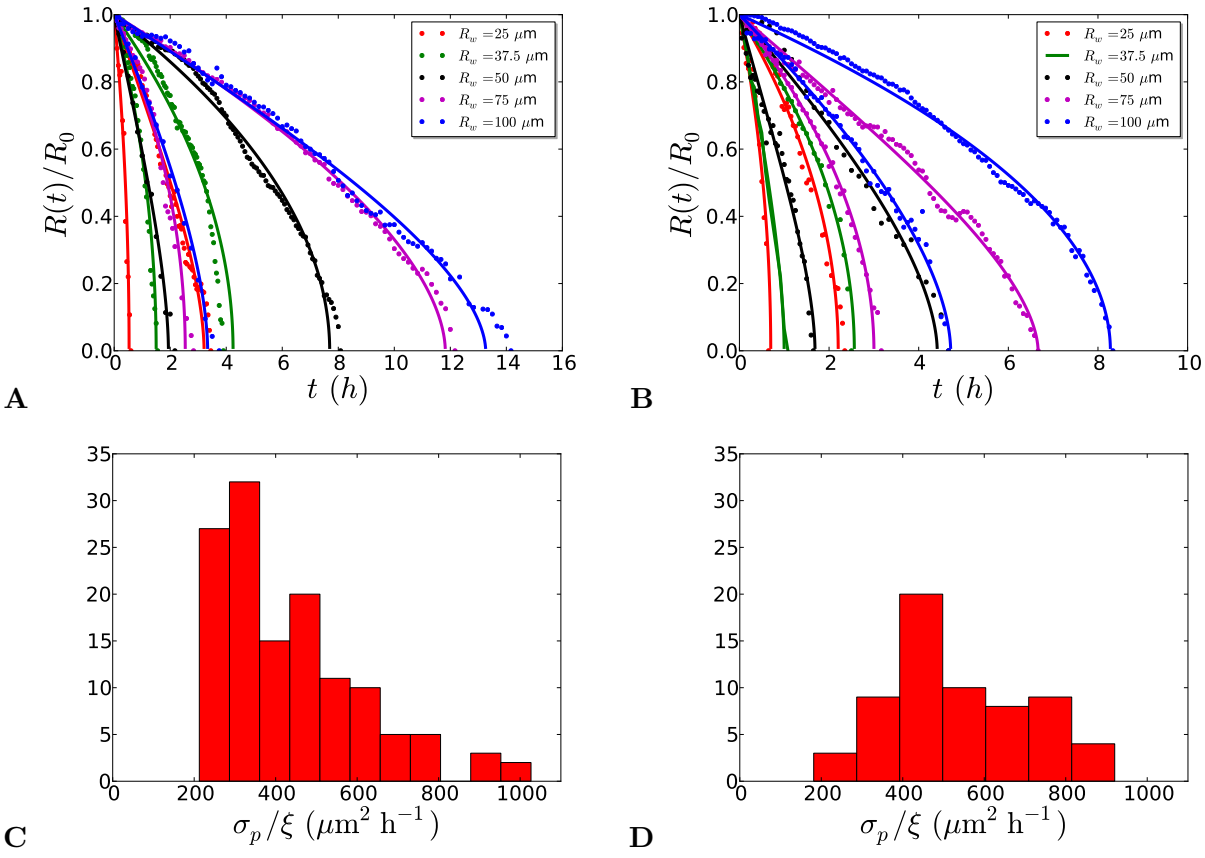

FIG. 10. **Trajectories $R(t)$ of closing wounds. A, C:** MDCK wild type wounds; **B, D:** HEK-HT wounds.

A, B: Fit of trajectories $R(t)$ with Equation (11). For clarity, we show only two trajectories (circles) and their fits (solid curves) per pillar size R_{w}, corresponding to the shortest and longest closure time observed at a given R_{w}. The normalized effective radius $R(t)/R_0$ is plotted as a function of time t.

C, D: Histogram of estimates of the epithelization coefficient (see text for details).

values). The distributions of epithelization coefficients obtained by fitting Equation (11) to data are shown in Fig. 10, for MDCK-WT and HEK-HT wounds, with mean values ± standard deviations given by:

- MDCK wild type wounds: $\sigma_{\mathrm{p}}/\xi = 424 \pm 170\,\mu\mathrm{m}^2\,\mathrm{h}^{-1}$;
- HEK-HT wounds: $\sigma_{\mathrm{p}}/\xi = 522 \pm 165\,\mu\mathrm{m}^2\,\mathrm{h}^{-1}$.

For both cell types, the confidence intervals obtained from fitting closure time data belong to the above intervals: the two measurement methods are consistent. Trajectories are noisy, due to intrinsic variabity, but also to possible pixelization errors when determining the area of the cell-free domain. Fitting individual trajectories leads to a higher dispersion of estimated parameter values. We therefore prefer to use closure time data for parameter estimation whenever closure is complete.

2. Non-closing wounds

We finally turn to the non-closing wounds observed in MDCK Rac$^-$ assays. Among the models presented in Section I, the only case where the final radius is strictly positive is that of an elastic epithelium with $R_\mathrm{e} > 0$, or $2\mu > \gamma/R_0$. In Fig. 11A, we show that individual trajectories are fitted satisfactorily by Equation (26). The equilibrium radius R_e increases with the initial effective radius R_0 (Fig. 11B), as predicted by Equation (22). A linear regression of R_e vs. R_0 yields the estimates

$$\frac{2\mu}{2\mu+\sigma_\mathrm{p}} = 0.5 \pm 0.1 \tag{32}$$

$$\frac{\gamma}{2\mu+\sigma_\mathrm{p}} = 6 \pm 7\ \mu\mathrm{m}. \tag{33}$$

From (32), we deduce that $\mu/\sigma_\mathrm{p} \approx 0.5$. Assuming that the Rac pathway has a limited influence on the epithelial elasticity, this suggests that Rac inhibition leads to lower values of the protrusive stress (compared to wild type assays), of the order of the elastic modulus. Since $\mu/\sigma_\mathrm{p} \approx 0.5$, Equation (33) yields $R_\gamma \approx 10\,\mu$m: the actomyosin cable contributes significantly to force production in non-closing Rac$^-$ assays when, *e.g.*, $R_\mathrm{w} = 50\,\mu$m.

Fitting non-closing trajectories, we obtain estimates of the coefficient $D_s = D\left(1+\frac{2\mu}{\sigma_\mathrm{p}}\right)$. Using $\mu/\sigma_\mathrm{p} \approx 0.5$, we expect that $D \approx 0.5\,D_s$. In Fig. 11C, we plot the histogram of epithelization coefficients defined for simplicity as $D = 0.5\,D_s$. We find $\sigma_\mathrm{p}/\xi = 180 \pm 45\,\mu\mathrm{m}^2\,\mathrm{h}^{-1}$ (mean value $\pm$ standard deviation, $N = 29$). Fitting Rac$^-$ closing trajectories with Equation (11) for an inviscid epithelium, we obtain $\sigma_\mathrm{p}/\xi = 230 \pm 66\,\mu\mathrm{m}^2\,\mathrm{h}^{-1}$ ($N = 30$), a value slightly higher than the previous estimate obtained for non-closing wounds. Note that both estimates are consistent with that obtained from fitting time closure data.

A balance between driving forces at the margin and a bulk elastic restoring force explains the positive value of the equilibrium radius observed in these assays. A word of caution

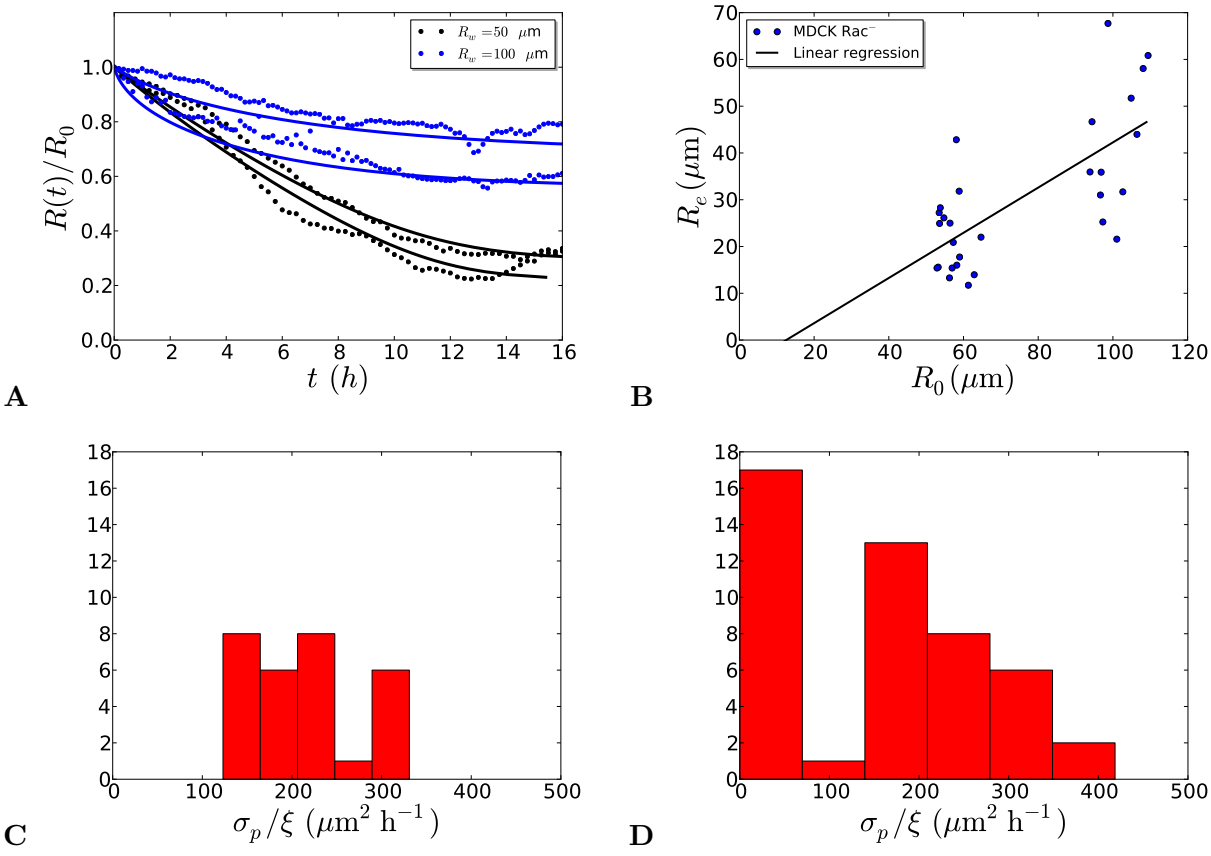

FIG. 11. **MDCK Rac$^-$ assay**

A-C: Non-closing wounds

A: Trajectories. Normalized effective radius $R(t)/R_0$ as a function of time t. For illustrative purposes, we show only two trajectories $t(R)$ per pillar size R_w (solid curves) and their fit by Equation (26) (dashed curves), with the constraints $D_S \geq 0$, $R_\mathrm{max} \in [96\ 114]\,\mu$m (confidence interval obtained from closure time data), $R_\mathrm{e} = \min R(t)$ (Equation (26) is defined only for $R > R_\mathrm{e}$).

B: Equilibrium Radius R_e (estimated as $R_\mathrm{e} = \min R(t)$) vs. initial radius R_0. The linear regression line (black solid line, $R_\mathrm{e} = aR_0 + b$) has coefficients $a = 0.5 \pm 0.1$, $b = -6 \pm 7\,\mu$m.

C: Histogram of parameter estimates. The epithelization coefficient is estimated as $D = D_s/2$ (from $2\mu/\sigma_\mathrm{p} \approx 1$), where D_s is obtained by nonlinear curve fitting of the trajectory, as in (a).

D: Closing wounds. Histogram of the epithelization coefficient. Closing trajectories are fitted as in Fig. 10A-B.

seems however in order. Although $R(t)$ plateaus on a time scale of the order of 15 h, one cannot exclude that a "non-closing wound" may in fact heal completely on a time scale much

longer than the available observation time, over which cell divisions may become relevant and need to be taken into account.

MOVIE 1. **Closure of a large MDCK circular wound.**
A MDCK-actin-GFP wound ($R_w = 250\,\mu$m) is imaged in epifluorescence for 14 h. Scale bar: $200\,\mu$m. Three leader cells formed at the edge of the wound and then drove multicellular fingers hence deforming the initial circle (Fig. 6). The fingers eventually met in the center and the leader cells switched back to a classical epithelial phenotype. The remaining secondary wounds then proceeded to heal in a much more regular fashion without showing any formation of leader cells (Movie 2).

MOVIE 2. **Closure of "secondary" wounds.**
Close-up on the secondary wounds from the experiment seen in Movie 1, imaged for 8.3 h. Scale bar: $100\,\mu$m. Neither leader cells and nor margin roughening are seen.

MOVIES 3-5. **Closure of small circular wounds.**
Three examples of time lapse movies made in phase contrast microscopy showing the typical closure of a wound for, respectively:

- wild type MDCK cells, $R_w = 50\,\mu$m for 6 h 30; scale bar: $100\,\mu$m;
- HEK-HT cells, $R_w = 50\,\mu$m for 4 h; scale bar: $100\,\mu$m;
- HEK-RasV12 cells, $R_w = 75\,\mu$m for 3 h 30; scale bar: $150\,\mu$m.

Direct inspection shows that the protrusive activity is enhanced in the last case, with a closure time shorter compared to a smaller wild type HEK wound.

MOVIE 6. **Dynamics of lamellipodial activity.**
A MDCK-LifeAct-GFP wound ($R_w = 25\,\mu$m) was imaged by confocal microscopy for 3 h. Scale bar: $25\,\mu$m. The optical slice was very close to the surface as this is the position where lamellipodia develop. For this reason, stress fibers were apparent but the membranes between cells were not. We observed a high number and a large activity of these lamellipodia that could be recognized as waves of actin in the bulk of the tissue. Of note, high laser power was needed to observe these lamellipodia and the dynamics of closure was drastically reduced in those experiments probably due to phototoxicity.

MOVIE 7. **Laser ablation of the entire cable.**
A MDCK LifeAct-GFP wound ($R_w = 25\,\mu$m) is imaged by confocal microscopy from $t = 30$

min after removal of the pillars. The actin cable is then fully ablated and the retraction of the edge is imaged for 1 min. Note the dynamic retraction of the edge of the wound. Scale bar : 10 μm.

MOVIE 8. **A non closing MDCK Rac$^-$ wound.**
A MDCK wound ($R_w = 50\,\mu$m) under Rac inhibition was imaged in phase contrast. The movie runs for 17.5 h. Scale bar: 100 μm.